Nano-Micro Letters

REVIEW

Core–Shell Semiconductor-Graphene Nanoarchitectures for Efficient Photocatalysis: State of the Art and Perspectives

Jinshen Lan[1], Shanzhi Qu[1], Xiaofang Ye[1], Yifan Zheng[1], Mengwei Ma[1], Shengshi Guo[1], Shengli Huang[1] ✉, Shuping Li[1] ✉, Junyong Kang[1]

HIGHLIGHTS

- The constructions under internal and external driving forces were introduced and compared with each other.

- The physicochemical properties were analyzed for the assessment of crystalline quality and photoelectric characteristics.

- The photocatalytic applications, mechanisms, and developments of the core-shell semiconductor-graphene nanoarchitectures were illustrated in detail.

ABSTRACT Semiconductor photocatalysis holds great promise for renewable energy generation and environment remediation, but generally suffers from the serious drawbacks on light absorption, charge generation and transport, and structural stability that limit the performance. The core–shell semiconductor-graphene (CSSG) nanoarchitectures may address these issues due to their unique structures with exceptional physical and chemical properties. This review explores recent advances of the CSSG nanoarchitectures in the photocatalytic performance. It starts with the classification of the CSSG nanoarchitectures by the dimensionality. Then, the construction methods under internal and external driving forces were introduced and compared with each other. Afterward, the physicochemical properties and photocatalytic applications of these nanoarchitectures were discussed, with a focus on their role in photocatalysis. It ends with a summary and some perspectives on future development of the CSSG nanoarchitectures toward highly efficient photocatalysts with extensive application. By harnessing the synergistic capabilities of the CSSG architectures, we aim to address pressing environmental and energy challenges and drive scientific progress in these fields.

✉ Shengli Huang, huangsl@xmu.edu.cn; Shuping Li, lsp@xmu.edu.cn
[1] Engineering Research Center of Micro-Nano Optoelectronic Materials and Devices, Ministry of Education, Fujian Key Laboratory of Semiconductor Materials and Applications, CI Center for OSED, Department of Physics, Xiamen University, Xiamen 361005, People's Republic of China

1 Introduction

The environmental and energy challenges have become critical global issues for the rapid development of economy and social activity in the twenty-first century. The semiconductor photocatalysts emerge as a solution as they can directly convert solar energy into chemical energy as well as catalytically degrade organic pollutants into harmless substances and renewable fuels [1–3]. However, single semiconductor materials often suffer from poor solar absorption, low generation rate of the electron–hole pairs, fast charge recombination and structural instability that restrict their performances. To overcome these shortcomings and unlock the full potential of semiconductors, heterogeneous engineering, elemental doping and surface modification have been widely adopted [4–12]. In particular, the construction of core–shell nanoarchitectures has gained prominence due to its large heterojunction area with exceptional chemical and physical properties, which allows for the enhancement and modification of material properties through the synergy of the different components [13–16].

Graphene, as a unique hexagonal sp^2 hybrid carbon network, has an extraordinary surface area of 2630 m^2 g^{-1}, a high charge carrier mobility of 2×10^5 cm^2 V^{-1} S^{-1}, an exceptional thermal conductivity of 5000 W m^{-1} K^{-1}, a good optical transparency efficiency of 97.7%, superior mechanical properties with a large Young's modulus exceeding 1.0 TPa, and strong chemical stability [17–21]. These unique characteristics make graphene and its derivatives (graphene oxide and reduced graphene oxide) an indispensable choice in the semiconductor modification, sparking significant interest in the field of solar cell [22, 23], lithium-ion battery [24–27], supercapacitor [28, 29], photodetector [30, 31], and photocatalysis [32–35]. In contrast to other structures, the core–shell semiconductor-graphene (CSSG) nanoarchitectures own a large junction area with a built-in electric field, which promotes electron–hole pair separation in the semiconductor component and directs charge migration from semiconductor to the conductive graphene. Secondly, the CSSG nanoarchitectures can intensify or introduce new chemical or physical capabilities not present in the individual core and shell materials, such as the formation of C-metal bonds that change the optoelectronic properties of the semiconductor component [36, 37]. Thirdly, the shell can act as a protective layer that maintains the structural integrity and properties of the core by excluding environmental influence, limiting volume expansion and preventing aggregation into large particles. Fourthly, the CSSG nanoarchitectures can significantly improve light absorption and utilization for the transparent characteristic of the graphene sheets. Last but not the least, the CSSG nanoarchitectures can selectively percolate ions or molecules onto the core, allowing for controlled interactions. Thanks to these advantages and the rapid development of construction methods and characterization techniques, the CSSG nanomaterials have been synthesized in various morphologies and gained considerable achievements.

Although tremendous efforts have been devoted to the fabrication and application of CSSG nanomaterials, much research interest was focused on a specific sample [36–40]. The related review is mainly devoted to the energy conversion and storage in lithium-ion batteries and supercapacitors [41–44], while that on photocatalysis is rarely reported. Given that the research on these hybrid materials is progressing fast, a review about the selection of appropriate fabrication methods to obtain desired CSSG nanoarchitectures based on the photocatalytic application is greatly needed. The suitability of photocatalytic system and the mechanism illustration should be carried out to promote the implementation of this technology. This review highlights the CSSG nanoarchitectures for photocatalytic performance. Specifically, the section following introduction, i.e., Sect. 2, classifies the CSSG nanoarchitectures by the dimensionality. In Sect. 3, the construction methods of the CSSG nanoarchitectures are introduced and compared with each other. In Sect. 4, the physicochemical properties of the CSSG nanoarchitectures are analyzed, with a focus on the binding effect, the amount and lattice characteristics of the graphene sheets, the photoelectric modulation of the semiconductor component, the defect states and charge transport of the hybrid materials. In Sect. 5, the photocatalytic applications of the CSSG nanoarchitectures, including the degradation of organic pollutants, the generation of hydrogen gas, and the reduction of carbon dioxide are discussed, where the photocatalytic mechanisms are illustrated in order to reveal the enhancement. In Sect. 6, a summary and future developments of the CSSG nanoarchitectures on photocatalysis are provided.

2 Classification of CSSG Nanoarchitectures

The CSSG nanoarchitectures can be divided based on the dimensionality, including 0-dimension (0D), 1-dimension (1D), 2-dimension (2D) and 3-dimension (3D), as presented in Scheme 1. The CSSG nanoarchitecture in 0D contains the morphologies of particle, sphere, quantum dot (QD), quasi-sphere and quasi-particle [36, 38, 45–49], while that in 1D presents in the forms of wire, rod, fiber, and tube [38, 40, 50–59], and that in 2D dominates in the morphologies of thin film and nanosheet [60–63]. The CSSG nanoarchitecture in 3D appears in diverse morphologies, such as rose, walnut, urchin, and hollow sphere [37, 64–70]. However, the 3D architecture is generally constructed by the 0D, 1D, or 2D materials. For example, the flower-like configuration of c-Ga$_2$O$_3$@rGO core–shell nanostructures is composed of 2D nanosheets [68]. In the CSSG nanoarchitectures, the semiconductor component may be in the core or in the shell, or the graphene sheet inserts among the semiconductor component. Except for the semiconductor and graphene, other chemical components may be also included for the enhanced performance, such as noble metal nanoparticles (NPs) [52, 71]. The graphene can be single- or multilayered graphene nanosheets, graphene oxide or reduced graphene oxide. For simplification, in the following discussion, the graphene refers to the graphene and its derivatives, while the G, GO, and rGO refer to the specific graphene, graphene oxide, and reduced graphene oxide.

For the photocatalytic application, the 0D CSSG catalysts own a large specific surface area and a stable structure, which are beneficial for the reactant absorption and recyclability. Nevertheless, the catalysts are generally dispersed in the solution, thus are hard to be recovered, and may induce secondary pollution. The 1D and 2D CSSG catalysts may be designed as an array standing on the substrates [40, 60]. This can be reused conveniently just by immersing the substrates in the solution and picking up, but the array uniformity may be limited by the construction method. The 3D CSSG catalysts can expand orientations with large interface area, but the structural stability and accessible surface-active sites need to be considered. The designed components and structures should be based on the material function, recyclability, and viable synthesis methods.

3 Construction Methods

The CSSG nanomaterials have been constructed by a lot of methods that are driven by the internal force or external force. For example, most of the CSSG nanomaterials are synthesized by the electrostatic self-assembly, which is due to the internal force of electrostatic interparticle attraction [21, 69, 72–77]. On the other hand, the CSSG nanomaterials with perfect crystalline characteristics are widely fabricated by chemical vapor deposition (CVD) that can be considered as the external force for the high-temperature and gaseous environment [20, 36, 60, 78, 79]. Nevertheless, the both kinds of driving force may coexist in the synthesis of a specific sample. In this section, the widely adopted construction methods of the CSSG nanomaterials will be introduced, and the advantages and disadvantages of each method will be disclosed in detail.

3.1 Electrostatic Self-Assembly

The electrostatic self-assembly is a widely adopted method in the synthesis of CSSG nanomaterials. It may consist of three steps, as shown in Fig. 1a [37]. Firstly, the semiconductor surface is modified with a positive potential. Secondly, a GO layer coats onto the semiconductor by the electrostatic attraction between the positive potential of semiconductor and the intrinsic negative potential of GO [80]. Lastly, the GO shell is converted to graphene. In the first step, the poly(allylamine hydrochloride) (PAH) solution or aminopropyl-trimethoxysilane solution (APTES) can be used as the modifier to induce the cationic surface of the semiconductor [38, 40, 72, 81], while in the last step, the reduction can be performed by annealing at high temperatures or by reduction agents, such as hydrazine [40, 54]. As the electrostatic attraction plays a critical role in the core–shell coupling, this method can be considered as driven by the internal force. The whole process can be carried out in solution, which is convenient for the operation, for different components and morphologies, and for a large scale. Nevertheless, it is difficult to control interfacial growth, and the residuals of the molecular linkers may counteract the performance. In order to reduce or exclude the negative effects of molecular linkers, further action can be taken on the achieved samples, such as thermolysis, acid modulation, and isotope substitution [57, 82, 83].
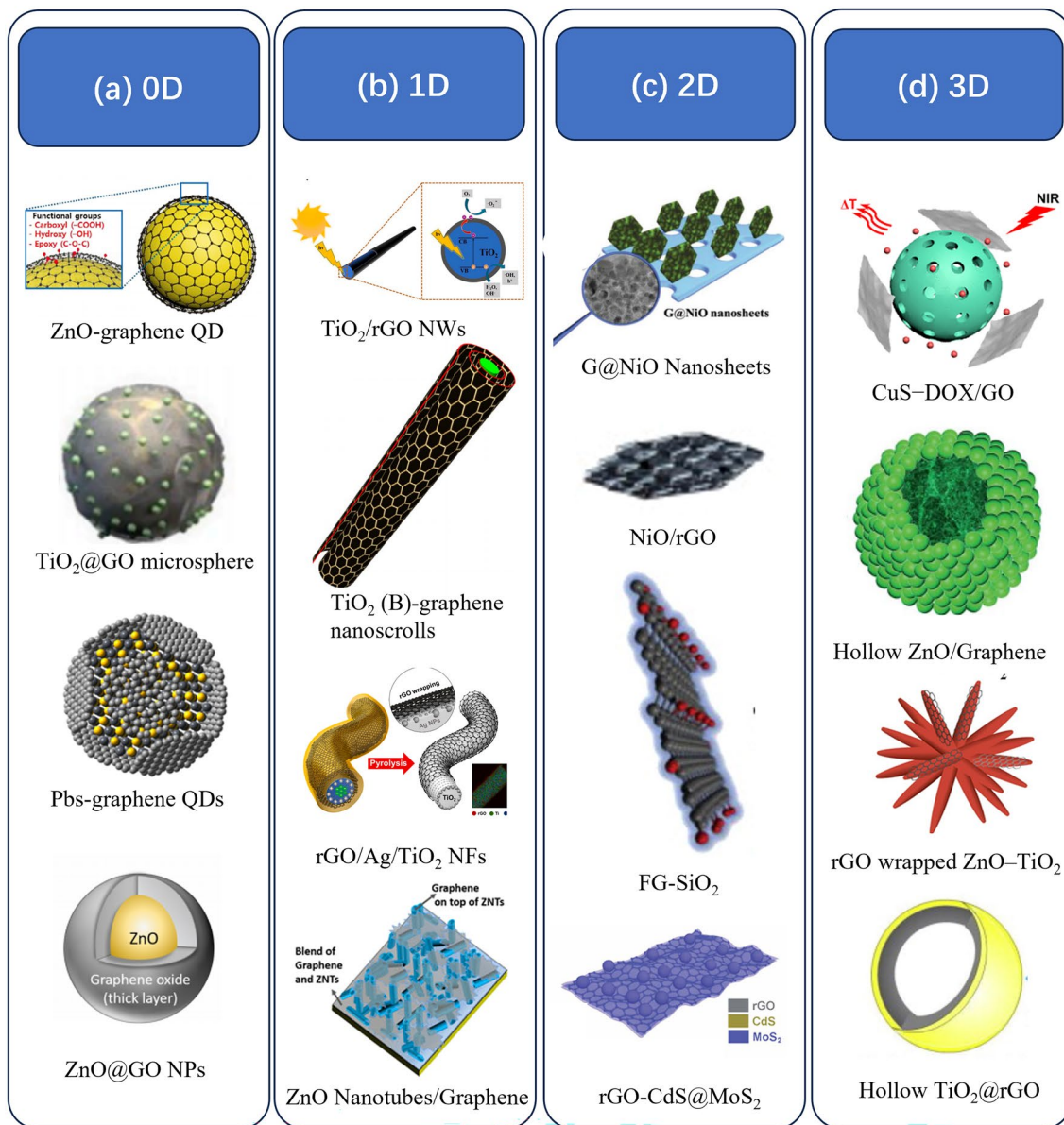
Scheme 1 CSSG nanomaterials in 0D, 1D, 2D, and 3D architectures. **a** 0D nanostructure of ZnO-Graphene quantum dots (reproduced with permission from Ref. [45]. Copyright 2021 Elsevier Publishing), TiO$_2$@GO microsphere (reproduced with permission from Ref. [46]. Copyright 2022 Elsevier Publishing), PbS/G QDs (reproduced with permission from Ref. [47]. Copyright 2015 ACS Publishing), ZnO@GO NPs (reproduced with permission from Ref. [48]. Copyright 2020 Elsevier Publishing); **b** 1D nanostructure of TiO$_2$/rGO NWs (reproduced with permission from Ref. [50]. Copyright 2022 Elsevier Publishing), TiO$_2$ (B)-graphene nanoscrolls (reproduced with permission from Ref. [51]. Copyright 2014 Elsevier Publishing), rGO/Ag/TiO$_2$ NFs (reproduced with permission from Ref. [52]. Copyright 2022 Elsevier Publishing), ZnO Nanotubes/Graphene (reproduced with permission from Ref. [53]. Copyright 2017 ACS Publishing); **c** 2D nanostructure of G@NiO Nanosheets (reproduced with permission from Ref. [60]. Copyright 2017 WILEY–VCH Publishing), NiO/rGO (reproduced with permission from Ref. [61]. Copyright 2019 Elsevier Publishing), FG-SiO$_2$ (reproduced with permission from Ref. [62]. Copyright 2014 Elsevier Publishing), rGO-CdS@MoS$_2$ (reproduced with permission from Ref. [63]. Copyright 2021 RSC Publishing); **d** 3D nanostructure of CuS−DOX/GO (reproduced with permission from Ref. [64]. Copyright 2017 ACS Publishing), Hollow ZnO/Graphene (reproduced with permission from Ref. [65]. Copyright 2016 RSC Publishing), rGO wrapped ZnO–TiO$_2$ (reproduced with permission from Ref. [66]. Copyright 2021 MDPI Publishing), Hollow TiO$_2$@rGO (reproduced with permission from Ref. [67]. Copyright 2015 Elsevier Publishing)
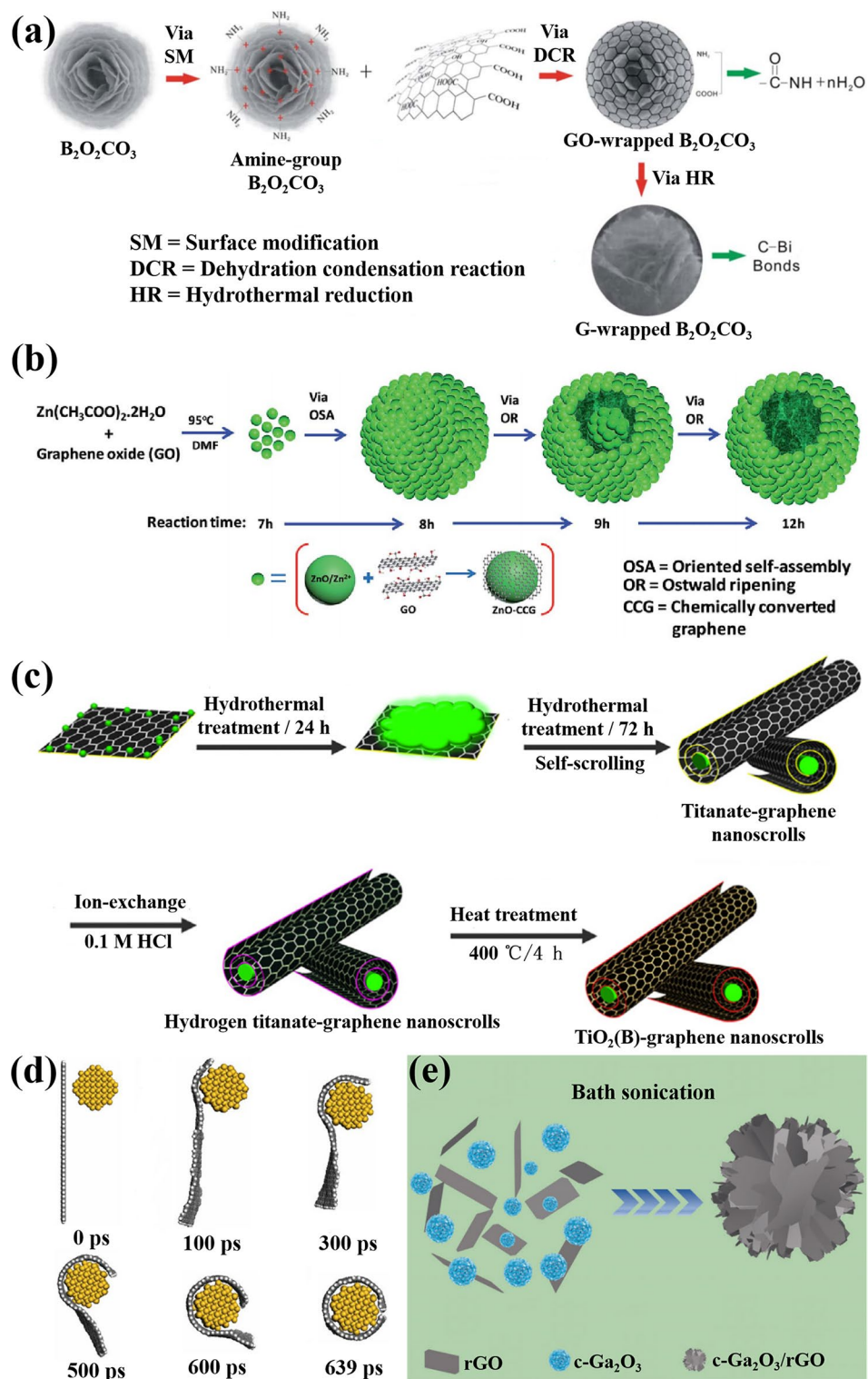
Fig. 1 Construction methods of the CSSG nanoarchitectures by the internal force: **a** Electrostatic self-assembly (reproduced with permission from Ref. [37]. Copyright 2014 RSC Publishing). **b** Oriented self-assembly and Ostwald ripening (reproduced with permission from Ref. [65]. Copyright 2016 RSC Publishing). **c** Hydrothermal treatment and self-scrolling (reproduced with permission from Ref. [51]. Copyright 2014 Elsevier Publishing). **d** Van der Waals interaction (reproduced with permission from Ref. [59]. Copyright 2010 Elsevier Publishing). **e** Bath sonication (reproduced with permission from Ref. [68]. Copyright 2023 Wiley Online Library Publishing)

3.2 Oriented Self-Assembly and Ostwald Ripening

The process of oriented self-assembly and Ostwald ripening is a hydrothermal method that can produce CSSG nanomaterials with various morphologies in solid and hollow microspheres (MSs). As displayed in Fig. 1b [65], the core–shell ZnO/graphene NPs are achieved by the covalent reaction of zinc acetate dihydrate and GO in dimethyl formamide (DMF) medium. The NPs start to aggregate preferentially and self-assemble into metastable MSs by oriented attachment to minimize the total surface energy. On prolonging the reaction time, the solid MSs convert into core–shell structured hollow MSs and finally, to hollow MSs by the loss of smaller NPs into larger NPs via Ostwald ripening process. In this method, the formation of the CSSG nanomaterials is merely driven by the covalent reaction as the internal force, and the various morphology can be achieved in the same solution by just optimizing the reaction time and temperature, which is more convenient than that for electrostatic self-assembly. However, the covalent reaction at the low temperature is only possible for some active specific reactants, which limits the material choice. Moreover, the oriented self-assembly and Ostwald ripening induce difficulty in structure control of the final product. The external force, such as an electric or magnetic field, can be applied to direct the growth orientation and increase the crystal quality [84].

3.3 Hydrothermal Treatment and Ion-Exchange/ Self-Scrolling/Self-Stocking/Annealing

The method uses the amphiphilic and self-scrolling nature of the GO nanosheets as the internal force [59, 85]. As illustrated in Fig. 1c [51], the titania NPs are likely to anchor on the GO nanosheets to form homogeneous suspension in alkali solution under ultrasonication. After hydrothermal treatment, the amorphous titanate intermediates successively contract and transform to titanate nanowires (NWs), while the graphene nanosheets are scrolled up to encapsulate titanate NWs inside. After ion-exchange and annealing, the core–shell titanate/graphene NWs are synthesized. The final annealing can be performed in solution [86–90], air [51, 91], vacuum [92], or special gas atmosphere [80], which plays an important role in improving the crystal quality and interfacial affinity between the core and the shell. As it is a one-step hydrothermal method, the operation is simpler than the others, and the product can be acquired in any amount and morphology. Nevertheless, the reaction should take place at a high temperature, generally close to the temperature capability of an autoclave. In addition, the reactants may act as the residue in the products, and the final morphology is also uncontrollable as it is a spontaneous process.

3.4 Van Der Waals Interaction

The method limits to the adjacent small objects. As shown in Fig. 1d [59], once the diameter of the NWs (yellow dots) reaches a threshold (10 nm), the surface adsorption stress of the NWs, which comes from van der Waals force as an internal driver, is introduced to bend graphene nanosheets to roll up and cover on the NW surface. This construction takes place in solution and can be modulated by the solute concentration and temperature [58], which is convenient for the operation. However, the shell thickness is difficult to be modulated, and the interface may be loose for the weak binding. Surface modification may be applied to improve the interaction and binding force between the core and the shell.

3.5 Bath Sonication

The CSSG nanomaterials grown by bath sonication generally use the natural opposite zeta potentials of reactants as the internal force for the core and shell. As shown in Fig. 1e [68], the zeta potentials of c-Ga_2O_3 and rGO are $+48.6$ and -58.3 mV, respectively. When the two components are dispersed in the solution by the sonication, they will assemble into a flower-like configuration of c-Ga_2O_3/rGO core–shell nanostructures for the electrostatic attraction. The experiment is usually performed in the solution at room temperature [68, 93, 94], which is much easier than others. However, the potential difference of the components should be as large as possible, so that they can exclude interference and combine together with an intimate interface. Moreover, the shell thickness is difficult to be increased as the electrostatic force will be reduced for the long distance.

3.6 Chemical Vapor Deposition

The chemical vapor deposition (CVD) is widely adopted to grow CSSG nanomaterials in different component with

different morphology in a high quality. In a general process, the semiconductor compound is loaded in a quartz tube. Then, the tube is heated to a reaction temperature. Afterward, the hydrogen and argon gases are introduced to the reactor for some time in order to clean and activate the semiconductor surface. Finally, the gas-phase carbon source (methane, ethylene, etc.) is also introduced to the reactor for the graphene growth. Therefore, the CVD is mainly driven by the external force for the high-temperature and gaseous environment. The thickness of the graphene shell can be modulated by the reaction time, temperature and gas flux. It is conjectured that the semiconductor surface will produce dangling bonds in the gas atmosphere at high temperatures, which will stick strongly to the C atoms from the decomposed hydrocarbons. The surface-adsorbed C atoms accumulate to form graphene. The hydrogen gas is not indispensable for the reaction, but it can reduce the reaction temperature, produce more active sites on the semiconductor surface, and bring the formation of large-size graphene, as shown in Fig. 2a [95]. Because the gas sources tend to react with the oxygen in air, the experiment can only be performed in the sealed tubes.

3.7 Pyrolysis

The CSSG nanomaterials achieved from pyrolysis requires that the core semiconductor contains the carbon component, and the surface layer of the semiconductor inclines to decompose at high temperatures [19, 96]. As displayed in Fig. 2b [96], the surface of SiC particles decomposes into silicon and carbon atoms at high temperatures in argon atmosphere, leading to the escape of silicon atoms and the reconstruction of C ions to from a graphene layer on the particles. In the experiment, the temperature, acting as the external driving force, should be high enough to decompose the compound, and the performance needs to be in vacuum or inert gas to avoid the oxygen reaction.

3.8 Electrospinning and Annealing

Using a core–shell nozzle, the CSSG NWs or nanofibers (NFs) can be achieved by the electrospinning method [52, 56]. As displayed in Fig. 2c [52], a negative electric potential (− 15 kV) is placed between the nozzle and a collector. A polyvinylpyrrolidone (PVP)/rGO solution is ejected through
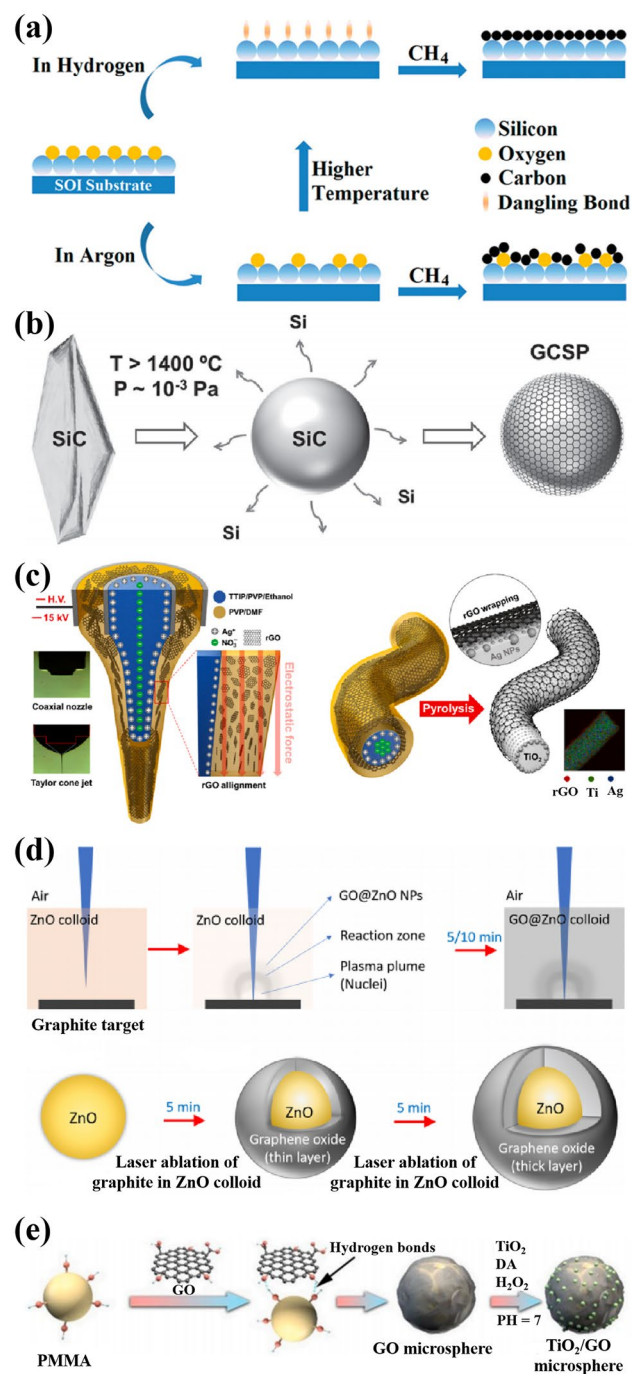

Fig. 2 Construction methods of the CSSG nanoarchitectures by the external or internal force: **a** CVD (reproduced with permission from Ref. [95]. Copyright 2012 AIP Publishing). **b** Pyrolysis (reproduced with permission from Ref. [96]. Copyright 2015 WILEY–VCH Publishing). **c** Electrospinning and annealing (reproduced with permission from Ref. [52]. Copyright 2022 Elsevier Publishing). **d** Laser ablation (reproduced with permission from Ref. [48]. Copyright 2020 Elsevier Publishing). **e** Template method (reproduced with permission from Ref. [46]. Copyright 2022 Elsevier Publishing)

the outer part of the nozzle and a AgNO$_3$/TTIP(Titanium isopropoxide)/PVP composite solution through the inner part. The electrohydrodynamic alignment of rGO and transportation of Ag$^+$ occur during the electrospinning process, constructing core–shell NFs. Subsequent thermal treatment induces interfacial assembly of the rGO flakes on the surface of Ag/TiO$_2$ NFs. By turning the components, the method is convenient to construct different CSSG NFs and NWs, even the graphene in the core. Moreover, as driven by the external force, the electrospinning process can be replaced by other strategy, such as microfluidic-spinning [57]. However, in order to obtain a steady structure out of the nozzle, the sheath and core fluids are usually mixed with polymers, such as PVP. This may introduce impurity and deteriorate the performance of the final products. The last thermal treatment seems more important to remove the polymers.

3.9 Laser Ablation

Laser ablation of graphite target immersed in semiconductor colloid/deionized water medium can lead to the formation of GO-encapsulated semiconductor NPs, which follows the thermal evaporation mechanism. As shown in Fig. 2d [48], laser ablation on graphite plate exfoliates carbon layers to produce plasma plume rich in C ions. The plasma-induced water vapor and ionized ZnO NPs from ZnO colloid interact with the ablated carbon ions, resulting in the assembly of the latter carbon species on the surface of ZnO NPs and formation of core–shell ZnO/GO. The process is mainly driven by the laser exfoliation as the external force. By changing the colloid components and extending carbon ablation, the heterogeneous materials and shell thickness can be changed, which is convenient for the modulation. However, the colloids should be small enough in order to be wrapped uniformly.

3.10 Template Method

The CSSG nanomaterials can also be achieved by depositing the components on a template. As shown in Fig. 2e [46], by using the poly(methyl methacrylate) (PMMA) sphere as a hard template, GO nanosheets spontaneously wrap the surface of PMMA spheres, as driven by the hydrogen bonding and van der Waals force as the internal force. On this basis, the TiO$_2$ NPs are directly immobilized onto GO MS surface by using the dopamine (DA) as bridge, thus obtaining the 3D TiO$_2$@GO core–shell sphere. This method is convenient to adjust the CSSG morphology by using the pre-designed template structure, and the solid cores can be turned into void by annealing or etching. However, the binder is introduced for the combination, which may decline the physicochemical properties of the CSSG materials. Further action, such as thermolysis and acid modulation, can be performed to remove the binders, as that in the electrostatic self-assembly.

Besides the methods described above, the CSSG nanomaterials can also be synthesized by other ways, such as sol–gel synthesis [97, 98], ball-milling [99], spray drying [100–102], microwave-assisted synthesis [103–105], and so on [106–108]. For comparison, the diverse methods as well as the advantages and disadvantages of each one are listed in Table 1. It is believed that more and more methods will be adopted, which will enrich the construction, diversify the pattern, and expand the application of the CSSG nanomaterials.

4 Physicochemical Properties

In comparison with the pristine semiconductors, the control of the CSSG nanoarchitectures can endow them with large surface area, abundant surface states, extended light harvesting, improved heat and electronic conduction, and even vectoring charge separation and migration, all of which are beneficial for their optoelectronic and photocatalytic performances. In this section, the structure characteristics of the CSSG nanomaterials, the method to test the layer number and interlayer spacing of the graphene nanosheets, the modulation of optical and electrochemical properties, and the assessment of bandgap, defect states, charge transport, and recombination rate will be provided by comparison and analysis of the morphology and structure, optical, and electrochemical properties of the CSSG nanoarchitectures.

4.1 Morphology and Structure

The morphologies of CSSG materials are closely related to the synthetic method. For example, by hydrothermal treatment and ion-exchange, graphene nanosheets can be

Table 1 The comparison of synthesis methods of CSSG materials

Synthesis methods	Advantages	Disadvantages	References
Electrostatic self-assembly	Solution processable, large scale	Residuals of the molecular linkers, difficult to control interfacial growth process	[21, 37, 38, 40, 72–77]
Hydrothermal treatment and ion-exchange /self-scrolling /self-stocking /annealing	Solution processable, large scale	Special reactants, residuals of the reactants, uncontrollable structure	[50, 55, 59, 80, 86–92]
Covalent reaction	Solution processable, large scale	Residuals of the molecular linkers	[106]
Oriented self-assembly and Ostwald ripening	Solution processable, large scale	Special reactants, uncontrollable structure	[65]
Van der Waals interaction	Solution processable, large scale	Limited shell thickness, weak binding at the interface	[59, 60]
Bath sonication	Solution processable, large scale	Special reactants, limited shell thickness	[93]
In situ reduction and dealloying	Solution processable, large scale	Residuals of the reactants, un-uniformity	[70]
Sol–gel synthesis	Solution processable, large scale	Residuals of the reactants	[97]
Chemical vapor deposition	Good crystallization, tunable dimension, immobilization	Energy-intensive, special circumstance	[20, 36, 60, 95]
Pyrolysis	Thin shell layer	Energy-intensive, special sample	[19, 96]
Spray drying	Easy operation, low cost	Mixed phases	[100–102]
Electrospinning and annealing	Easy operation, low cost	Mixed phases	[52, 56]
Microfluidic spinning and annealing	Easy operation, low cost	Mixed phases	[57]
Laser ablation	Good crystallization, tunable dimension	Energy-intensive, limited core size	[48]
Template	Tunable structure	Residuals of the binders	[46]
Microwave-assisted synthesis	Uniform distribution of energy inside the reaction vessel, energy saving, high reproducibility, and excellent control over experimental parameters	Residuals of the reactants,	[103–105]
Adsorption–deposition	Solution processable, large scale	Residuals of the binders, limited thickness	[107]
Precipitation	Solution processable, large scale	Residuals of the reactants, morphology uncontrollable	[108]
Ball-milling	Easy operation, large scale	Special reactants, residuals of the reactants	[99]

scrolled up to encapsulate titanate NWs inside, resulting in scrolled architectures. The heat treatment at low temperature (400 °C) induces a porous structure with a visible gap between the core and the shell (Fig. 3a) [51], while a tightly binding architecture is achieved at a high temperature (700 °C) (Fig. 3b) [50, 54]. Generally, by the construction methods at high temperatures, such as pyrolysis and CVD, the covered graphene layer is smooth and wraps the semiconductor core tightly with perfect contact interfaces, where the graphene monolayers can be clearly observed (Fig. 3c–e) [19]. However, for the hydrothermal growth and other construction methods at relatively low temperatures, the CSSG architectures usually display wrinkled and rough surface texture, though the layer number of the graphene can be also accurately controlled (Fig. 3f, g) [49, 109].

Except for electron microscopy, the crystal quantity and graphene content of the CSSG nanomaterials can also be examined by XRD patterns, Raman, and infrared spectra. As observed in Fig. 4a [70], the XRD pattern of GO shows an intense and a relatively weak diffraction peaks in the 2θ of 9.5° (001) and 19.0° (002), which are due to the oxygenated functional groups and the amorphous nature of GO, while for G and rGO, the XRD pattern also presents two diffraction peaks at 22.0° and 41.0° that are corresponding to (002) and (001) plane of the nanosheets. The peak position and intensity are changed with the depletion of functional
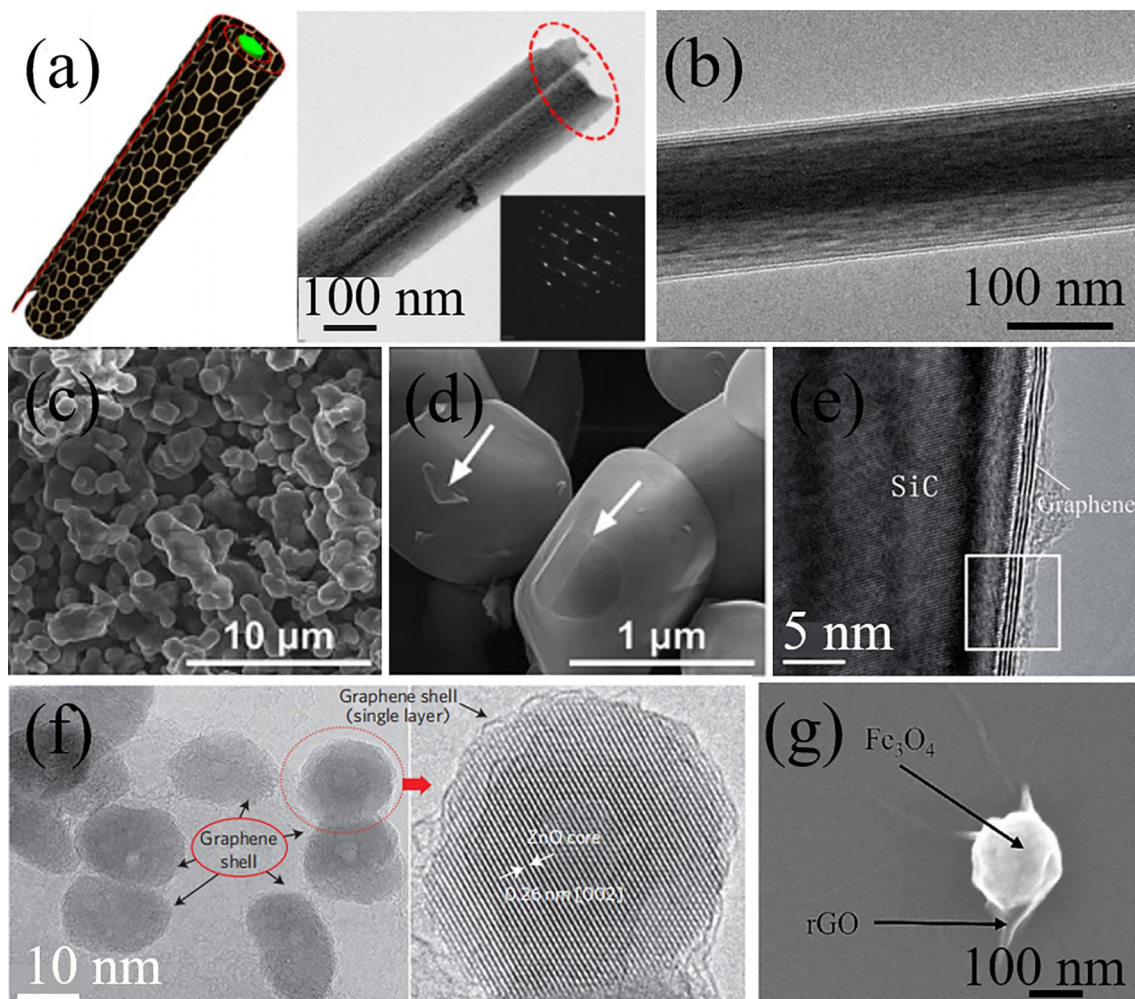
Fig. 3 Morphology and structure of the CSSG materials: **a** Structural illustration and TEM image of TiO_2 (B)-graphene nanoscrolls (the inset shows the corresponding SAED pattern) (reproduced with permission from Ref. [51]. Copyright 2014 Elsevier Publishing). **b** TEM image of a TiO_2/rGO NW. **c** SEM image of SiC/G NPs. **d** Magnified SEM image of SiC/G NPs (the arrows mark the peeled graphene or the graphene wrinkle). **e** HRTEM image of a SiC/G NP (reproduced with permission from Ref. [19]. Copyright 2014 RSC Publishing). **f** HRTEM image of ZnO/G QDs (reproduced with permission from Ref. [49]. Copyright 2012 Macmillan Publishers Limited Publishing). **g** SEM image of a Fe_3O_4/rGO NP (reproduced with permission from Ref. [109]. Copyright 2023 Elsevier Publishing)

groups, the exfoliation of multiple layers and the variation of interlayer spacing. The diffraction peaks of the graphene shell are generally depressed by the semiconductor core for the small amount of the shell layer. But for the CSSG nanomaterials with high crystal quality, the XRD pattern generally contains the diffraction peaks of the core and the shell (Fig. 4b) [49]. The average crystallite size, lattice parameters, and interplanar spacing of the core and the shell can be estimated from the patterns [38, 48, 110]. Kulinich et al. found that the graphene layers formed atop ZnO cores can reduce the density of defects and disorders, decrease the anisotropic tensile stress, and improve the crystallinity of

the ZnO cores [48]. However, these effects generally occur in the hard construction condition (laser ablation, pyrolysis, CVD, high-temperature annealing). In the mild conditions (electrostatic self-assembly, hydrothermal growth, etc.), the crystal features of the semiconductor cores are rarely influenced by the coating layers.

Raman scattering is commonly used to characterize carbon-based materials. Except for the scattering peaks of the semiconductor cores, Raman spectra of the CSSG nanomaterials contain characteristic bands of the graphene shells that are sensitive to the structural quality and layer number of the graphene as well as the interaction between
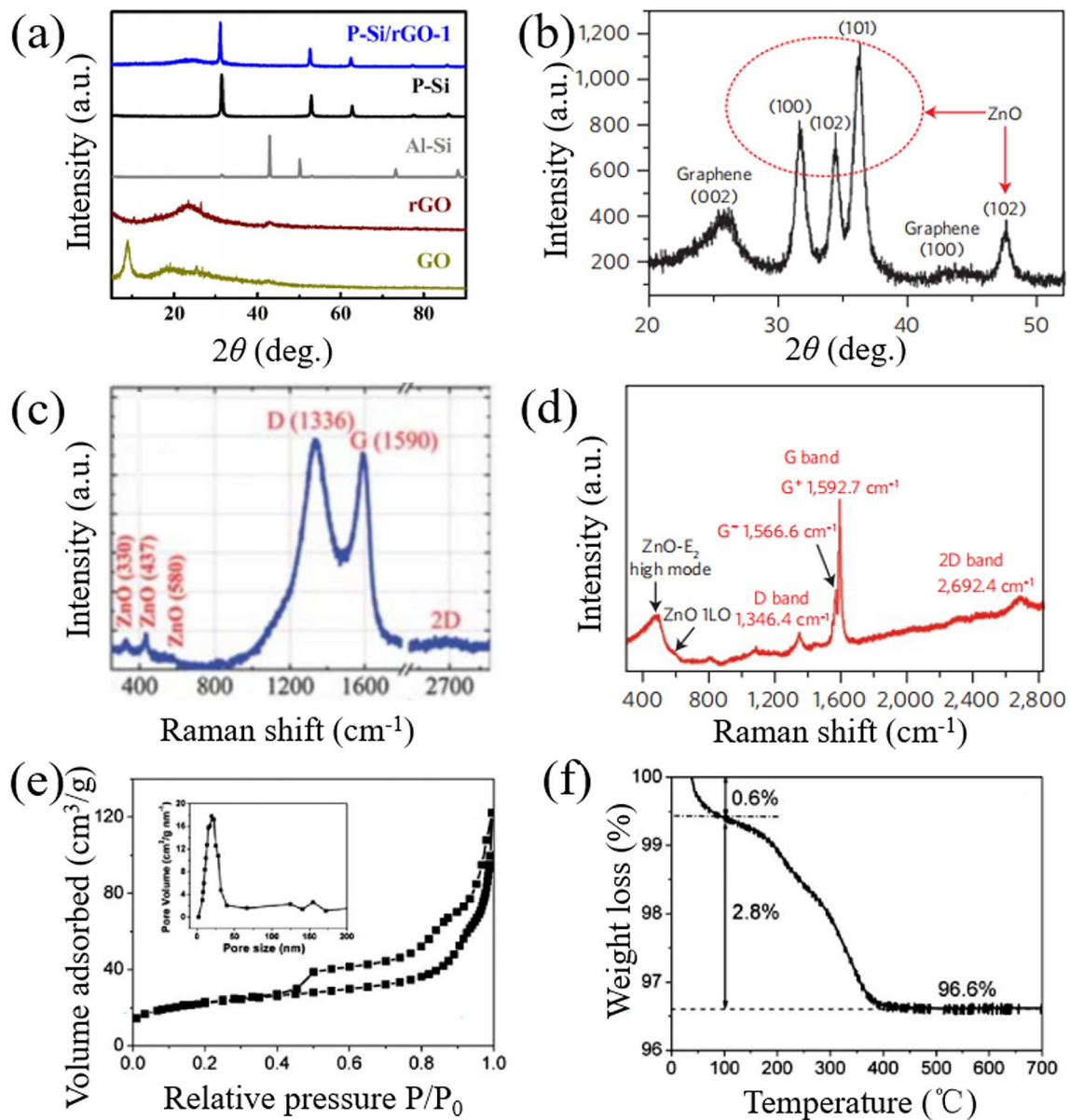
Fig. 4 Structural analysis of the CSSG materials: **a** XRD patterns of GO, rGO, Al-Si powder, porous Si, and porous Si/rGO (reproduced with permission from Ref. [70]. Copyright 2017 Tsinghua University Press and Springer-Verlag Berlin Heidelberg Publishing). **b** XRD pattern of ZnO/G QDs (reproduced with permission from Ref. [49]. Copyright 2012 Macmillan Publishers Limited Publishing). **c** Raman spectra of ZnO/G NPs (reproduced with permission from Ref. [38]. Copyright 2013 RSC Publishing). **d** Raman spectra of ZnO/G QDs (reproduced with permission from Ref. [49]. Copyright 2012 Macmillan Publishers Limited Publishing). **e** Nitrogen isotherm adsorption–desorption curve of a-Fe$_2$O$_3$/G NPs. (The inset shows their pore size distributions.) **f** Thermogravimetric analysis of a-Fe$_2$O$_3$/G NPs (reproduced with permission from Ref. [40]. Copyright 2011 RSC Publishing)

the core and the shell. Figure 4c shows the Raman spectra of ZnO/G NPs [102], where the dominate D band (1336 cm^{-1}) is corresponding to the non-sp^2 carbon bonding such as atomic-scale defects or lattice disorder of graphene, while the G band (1590 cm^{-1}) and 2D band (2675 cm^{-1}) are the characteristics of sp^2 hybridization of the C–C/C=C bonds in graphene. The intensity of G band and 2D band can be used to determine the number of graphene layers, whereas the intensity ratio of D band to G band (I_D/I_G) indicates disorder or local defects in the graphene layers that is widely applied

in the assessment of the crystal quality. Chen et al. found a clear increase of I_D/I_G from 0.95 for GO to 1.44 for G in hematite/G NPs, which is attributed to the formation of new and smaller sp^2 domains during the reduction [91]. Zhang et al. got an I_D/I_G ratio of 1.06 for commercial ZnO/G and 0.91 for hexagonal ZnO/G [72]. The difference suggests that the quality of graphene in hexagonal ZnO/G is higher than that in commercial ZnO/G and the structure of graphene in commercial ZnO/G is damaged in some degree after thermal annealing. The effect is also observed in TiO_2/G from TiO_2/GO by hydrothermal treatment [21]. Xu et al. found that the I_D/I_G ratio of Cu_2O/rGO is larger than that of GO nanosheets [90], demonstrating a decrease in the average size of the sp^2 domains upon reduction of the exfoliated GO. Kim et al. noticed that the I_D/I_G ratio of Al_2O_3/graphite decreased with increasing growth time, implying better multilayered graphene quality with the growth time [78]. Except for the intensity, the D and G bands will be shifted for the electronic interaction or electron transferring between the graphene shell and the semiconductor core. Moreover, both the double degenerate bands may divide into two sets of sub-bands (Fig. 4d) [49], D^+ and D^- as well as G^+ and G^-, due to the strain induced symmetry breaking of the bending graphene layer on the semiconductor surface, with polarization along and perpendicular to the strain.

One of the important roles of the graphene sheets in the CSSG nanomaterials is to improve the surface area and modulate the pore size, which can be measured by the nitrogen isotherm adsorption–desorption curve (Fig. 4e) [40]. The surface area, pore volume, and average pore size can be determined by the Brunauer–Emmett–Teller (BET) analysis. As shown in Table 2, most of the CSSG nanomaterials have a larger surface area than the pristine semiconductors. For example, the surface area of $MnFe_2O_3$/GO NPs is 70.7 $m^2 g^{-1}$, which increases distinctly more than 8 times of the area of $MnFe_2O_3$ NPs (7.7 $m^2 g^{-1}$) [88]. Such high value may be due to the fact that the core–shell morphology raises the dispersion of the particles and reduces the stacking of GO nanosheets, which is a prerequisite for high electrochemical performance owing to the enhanced accessible area for the deposition of dye molecules and the exchange of the ions at the electrode–electrolyte interface. However, some CSSG nanomaterials with declining surface area are also observed, such as CdS/G NPs [80], TiO_2/G NPs [79], and $SrFeO_3$/boron-doped rGO (B-rGO) nanospheres (NSs) [89]. This

Table 2 Surface area S, pore volume V, and average pore size d of the pristine semiconductors and CSSG nanomaterials as achieved from BET analysis

Specimen	S ($m^2 g^{-1}$)	V ($cm^3 g^{-1}$)	d (nm)	References
a-Fe_2O_3/G NPs	79.5	–	20	[40]
ZnO core–shell hollow MSs	29.4	0.19	26.9	[65]
ZnO/G solid MSs	30.7	0.20	27.2	
ZnO/G core–shell hollow MSs	40.5	0.15	15.3	
ZnO/G hollow MSs	37.6	0.12	12.2	
TiO_2(B) NWs	47.2	–	–	[51]
TiO_2(B)/G NWs	51.1	–	1–4	
Cu_2O MSs	29.5	–	3.4–4.1	[90]
Cu_2O/rGO MSs	53.6	–	3.4–4.1	
CdS NPs	19	–	32.2	[80]
$CdS_{(-0.05)}$/G NPs	9	–	35.9	
$CdS_{(-0.1)}$/G NPs	10	–	30.2	
$CdS_{(-0.15)}$/G NPs	10	–	39.5	
$CdS_{(-0.2)}$/G NPs	9	–	40.0	
TiO_2 (P25) NPs	50	–	38	[79]
TiO_2 (rutile) NPs	24	–	38	
TiO_2/G-5 NPs	12	–	166	
TiO_2/G-10 NPs	9.8	–	150	
TiO_2/G-30 NPs	7.3	–	165	
TiO_2/G-45 NPs	9.6	–	190	
$Ni(OH)_2$/RGO NSs	154	–	3–4	[93]
γ-Ga_2O_3 hollow NSs	81.84	–	3–4	[68]
γ-Ga_2O_3@RGO hollow NSs	152.95	–	3–4	
ZnO QDs	9.214	0.19	86.4	[45]
ZnO/G QDs	11.819	0.19	64.0	
ZnO/$G_{multilayer}$ QDs	32.849	0.23	28.0	
$MnFe_2O_3$ NPs	7.7	–	–	[88]
$MnFe_2O_3$/GO NPs	70.7	–	30	
$SrFeO_3$ MSs	204.76	–	0.29	[89]
$SrFeO_3$/B-rGO MSs	200.404	–	0.16	

may originate from the aggregation of the particles during heat treatments, the slight increase in the particle size by the shell layer, and the obstruction of the particle pores by graphene formation. In view of other properties and functions, the graphene shell should be in an appropriate amount. The content can be determined by thermogravimetric analysis (Fig. 4f) [40]. The weight percent of carbon loss may begin from the evaporation temperature of water at 100 °C to the combustion of graphene at 740 °C.

4.2 Optical Properties

The light absorption ability is a critical factor that influences the performance of the compound as a photodetector or photocatalyst. By coating graphene shell, the light harvesting capability of the CSSG nanomaterials can be improved significantly, and the band-edge absorption of the semiconductor core can be adjusted to better match the required spectral range. For example, the ZnO/G NPs show an intense and broad background absorption in the visible light region, which is much stronger than the pristine ZnO NPs [72]. The phenomenon is also observed in other CSSG nanomaterials, which may be because the shell layers create mesopores with different pore size distributions. The light coming across the sample is prevented by the shell layer. For different specimens, there is a different optimal thickness for the strongest absorption (Fig. 5a) [80].

The bandgap of the compounds, as indicated by an absorption edge in the spectra, can be determined by Tauc's plots using the following equation [9, 111]:

$$(\alpha h\nu)^{1/n} = A(h\nu - E_g) \tag{1}$$

where α is the absorption coefficient, h is the Planck constant, ν is the light frequency, A is a proportionality constant, E_g is the bandgap energy, and n represents the type of bandgap with n = 0.5 and 2 for direct and indirect bandgap semiconductors, respectively. Zubair et al. found that the pure CdS owns a bandgap energy of 2.32 eV, while the bandgap is gradually narrowed as the graphene shell increases up to CdS-0.015G sample (Fig. 5b) [80]. The reduced bandgap is ascribed to the doping of carbon in the CdS matrix and the interaction of graphene and CdS. Peter et al. observed that the bandgap of TiO_2/G QDs is closely related to the particle size [74]. The size effect is also found in PbS/G QDs [47]. Kang et al. observed that the bandgap of TiO_2/rGO NFs is narrower than that of TiO_2 NFs (from 2.99 to 3.19 eV) [52]. The effect is attributed to the presence of Ti–O–C bonds, which link electrons on the surface of TiO_2 with unpaired π-electrons, causing the valence band of TiO_2 to shift higher. The above results indicate that the electronic energy of the semiconductor core can be modulated by the graphene shell, which can achieve high electron transfer rate and delay the charge recombination more effectively. Moreover, the interfacial defects of the semiconductor core that typically act as recombination centers can be reduced significantly, as observed by the steepened absorption edges in the spectra [65, 96].

Photoluminescence (PL) spectra are widely used to investigate the efficiency of charge carrier trapping and migration, and the behavior of photogenerated electron–hole pairs. The improvement of crystal structure and electronic properties of CSSG nanoarchitectures can be illustrated by the change of position, intensity and bandwidth of the PL spectra. For instance, Zhang et al. observed two emission peaks in the PL spectra of the commercial ZnO (CZO) and hexagonal ZnO (HZO) NPs (Fig. 5c) [72]. The strong peak at 398 nm is the band-edge emission resulting from the recombination of excitonic centers, while the relative weak peak at 465 nm is the bound excitons arising from the intrinsic defects such as oxygen vacancy. The two peaks are markedly depressed for the core–shell CZO/Gr and HZO/Gr NPs due to the introduction of graphene that eliminates the surface defects and accepts the photoinduced electrons. The reduced emission intensity of the CSSG nanoarchitectures relative to the pristine semiconductors is also observed in other samples [49, 50, 72, 96], presenting lower recombination and improving separation efficiencies of the electron–hole pairs. The bandwidth of the PL spectra is closely relative to the crystal quality. Lu et al. observed a narrowed PL band of the core–shell SiC/G compared to that of the pristine SiC for the reduced interfacial defects [96]. Tavakoli et al. found that the PL spectrum of PbS/G becomes broadening for the passivation of graphene that decreases the amount of midgap states of the PbS QDs, as supported by the density functional theory simulation and time-resolved PL measurements (Fig. 5d) [47]. It is known that the excitation-dependent PL behavior is usually observed in fluorescent carbon materials [74]. Except for the intrinsic band-edge emission that keeps stable at an identical wavelength position, the PL bands of the vacancy, impurity, and defect states are sensitive to the excitation light. As shown in Fig. 5e, f [74], the increasing excitation wavelength induces the continual redshift and suppression of the emission band of G QDs that act as a coating layer on the core–shell TiO_2/G NPs.

4.3 Electrochemical Properties

Electrochemical impedance spectroscopy (EIS) spectra can be used to evaluate the photoelectrochemical performance of the electrodes. The Nyquist plots of the CSSG electrodes usually exhibit a semicircle in the high-frequency region and a straight line in the low-frequency region, as typical
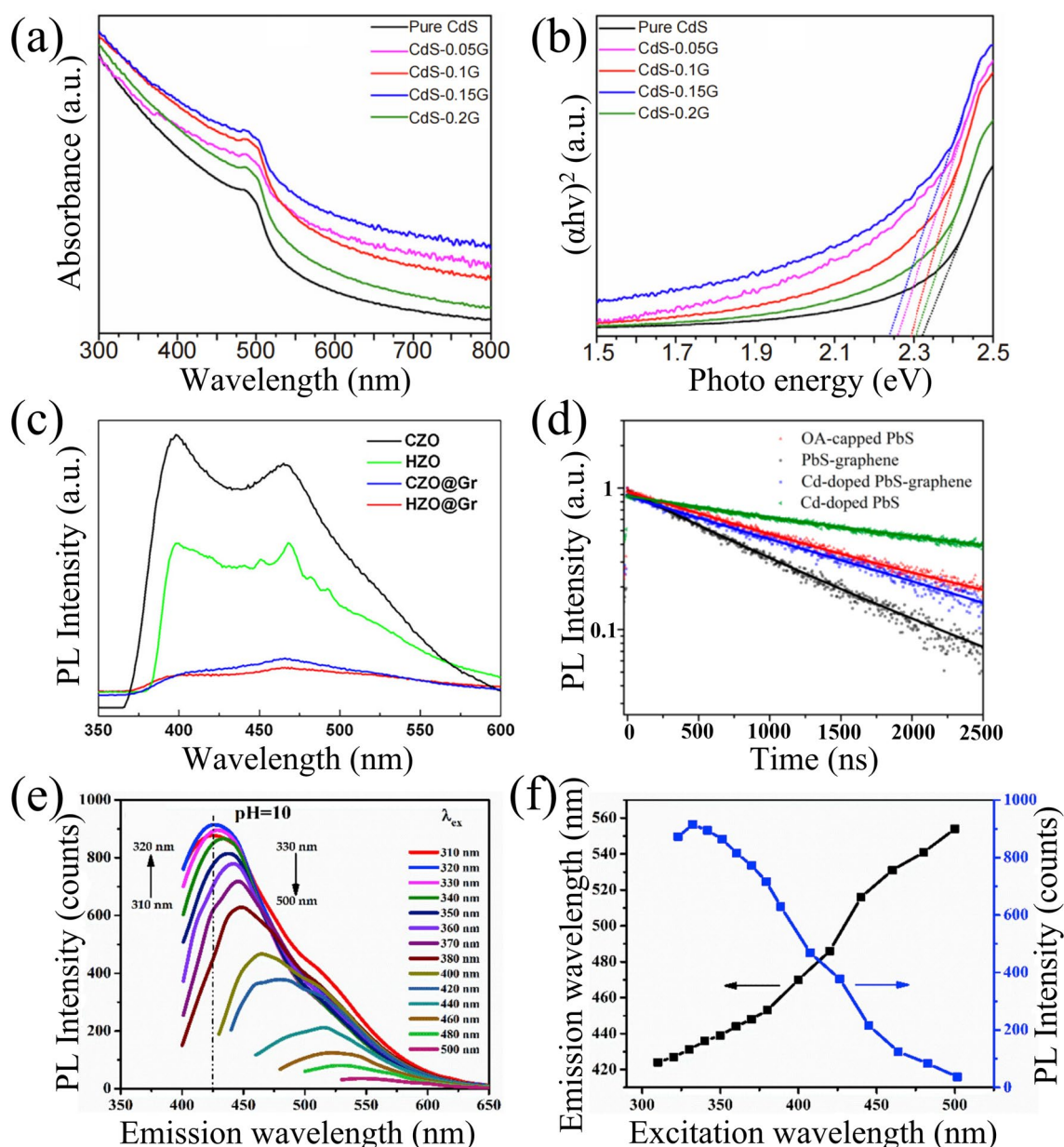
Fig. 5 Absorption and PL spectra of the CSSG materials: **a** UV–Vis absorption spectra and **b** optical bandgap calculations of pure CdS and C-doped CdS@G samples (reproduced with permission from Ref. [80]. Copyright 2020 KeAi Publishing). **c** PL emission of commercial ZnO (CZO), hexagonal ZnO (HZO), commercial ZnO@G (CZO@Gr), hexagonal ZnO@G (HZO@Gr) NPs (reproduced with permission from Ref. [72]. Copyright 2016 Elsevier Publishing). **d** PL decay curves of PS heterogeneous QDs (reproduced with permission from Ref. [47]. Copyright 2015 ACS Publishing). **e, f** Excitation-dependent photoluminescence spectrum of prepared G QDs (reproduced with permission from Ref. [74]. Copyright 2019 Elsevier Publishing)

examples in Fig. 6a, b [40, 90]. The semicircle is related to the electronic resistance and the charge transfer impedance R_{ct}. Bigger semicircle results in a large R_{ct} [20]. The contact point between the semicircle at the left side and the real axis is considered as the internal resistance of the electrode

material. Additionally, the linear type is mainly caused by Warburg impedance produced by the ion diffusion at the interface of the working electrode, which corresponds to the process of diffusion process. The steepest slope of the line indicates the best ion transport property. An ideal capacitor
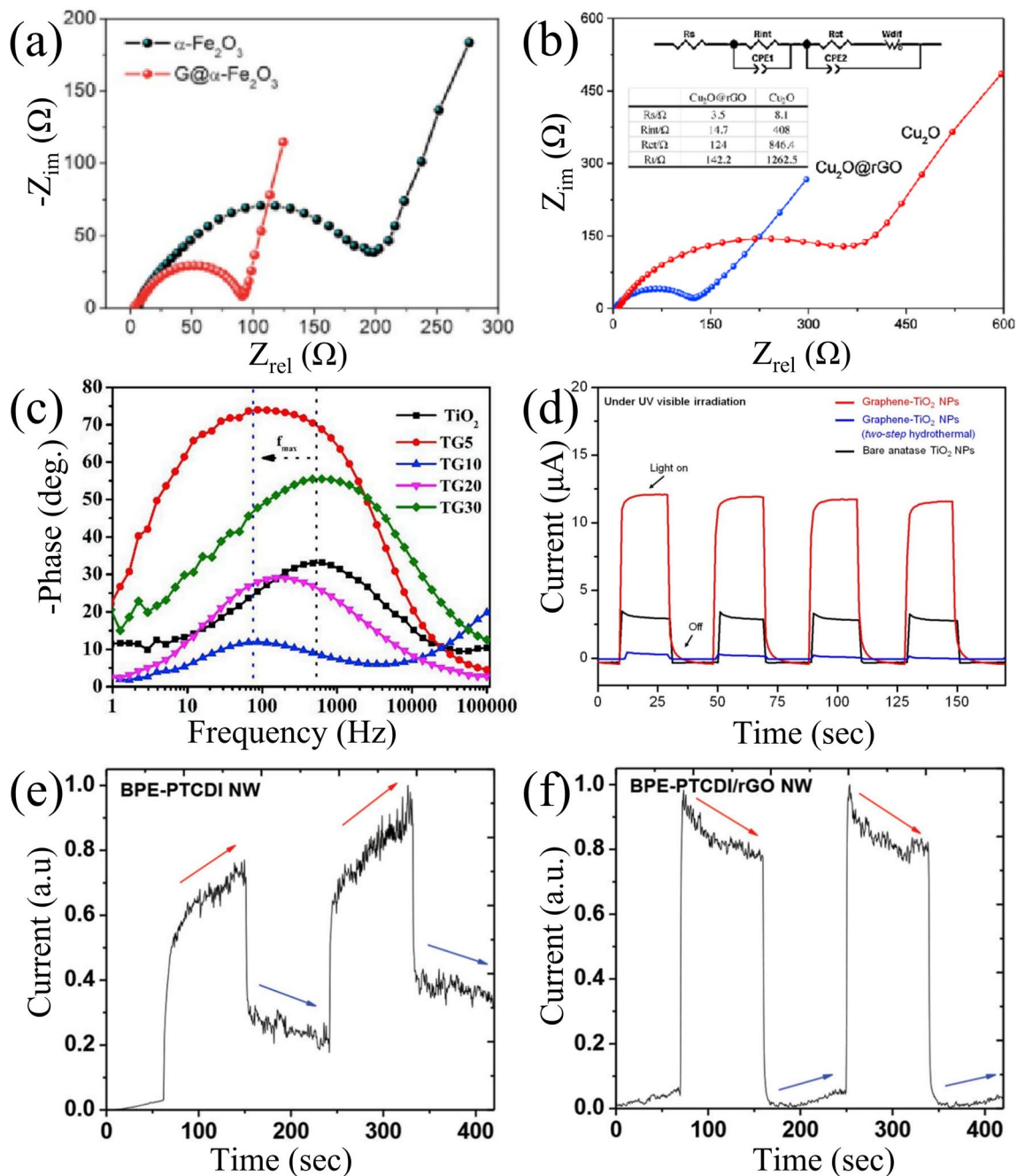
Fig. 6 Impedance and photocurrent of the CSSG materials: **a** Nyquist plots of a-Fe$_2$O$_3$@G and pristine a-Fe$_2$O$_3$ electrode (reproduced with permission from Ref. [40]. Copyright 2011 RSC Publishing). **b** Nyquist plots of Cu$_2$O@rGO and bare Cu$_2$O electrode (reproduced with permission from Ref. [90]. Copyright 2015 Elsevier Publishing). **c** Bode plots of TiO$_2$/G and pristine TiO$_2$ QDs electrode (reproduced with permission from Ref. [74]. Copyright 2019 Elsevier Publishing). **d** Photocurrent responses of bare anatase TiO$_2$ NPs, TiO$_2$/G NPs (two-step hydrothermal), and TiO$_2$/G NPs under UV–Vis irradiation (reproduced with permission from Ref. [21]. Copyright 2012 WILEY–VCH Publishing). Photocurrent responses of **e** BPE-PTCDI NWs and **f** BPE-PTCDI/rGO NWs (reproduced with permission from Ref. [58]. Copyright 2014 WILEY–VCH Publishing)

would show a vertical line. As shown in Fig. 6a [40], the semicircle diameter of α-Fe$_2$O$_3$/G is much smaller than that of α-Fe$_2$O$_3$, and the linear slope of the former is greater than the latter, demonstrating that the incorporation of graphene shell into the composite promotes electron transportation and ion diffusion and depresses the recombination of charge

carriers in the bulk, toward ideal capacitive behavior. The similar results are also observed in VO$_2$/G [87], Si/G [102], SrTiO$_3$/rGO [36], Ga$_2$O$_3$/rGO [68], and P-Si/rGO [70]. However, in some CSSG nanomaterials, such as Cu$_2$O/rGO in Fig. 6b [90], the ionic mobility changes little or even becomes worse as compared to the pristine semiconductors, though the R_{ct} is reduced. Zubair et al. found that the CdS/G electrode has the smallest diameter of the semicircle in light than the pure CdS electrode and all the samples in dark as well [80]. This indicates that the charge transfer resistance of the CSSG electrodes is influenced by the light irradiation.

Besides the impedance, the Bode plots as achieved in the EIS measurement allow comparing the electron lifetime, maximum phase angle, and relaxation time constant of the electrodes. Peter et al. found that the maximum frequencies (ω_{max}) in the middle frequency region of the Bode plots for pure and graphene QDs modified TiO$_2$ (TG10) are 613.13 and 75.77 Hz, respectively (Fig. 6c) [74]. Since ω_{max} is inversely related to the electron lifetime, the result reveals the significant increment of electron lifetime and the suppression of electron recombination of TG10. Yus et al. observed that the relaxation time constant of NiO/rGO electrode, as achieved from the Bode plots, is 4 ms lower than NiO-bare electrode (8 ms) [61], exhibiting a faster charge–discharge ability. However, the maximum phase angle declines from 76 degree of NiO-bare electrode to 70.4 degree of NiO/rGO electrode, indicating decaying capacity behavior. Moreover, the electrochemical performance of the NiO/rGO electrode can be modulated by the amount of rGO.

The photocurrent response is an effective way to detect the photoelectric conversion efficiency and separation efficiency of photoinduced electrons and holes. The intensity, rising, and falling edges of the photocurrent profile are closely relative to the band structure, charge density, impurity, and vacancy states of the working electrodes. Lee et al. found that the TiO$_2$/G NPs produce much higher photocurrent under ultraviolet (UV) light irradiation, at a rate approximately 17 times larger than that of the bare anatase TiO$_2$ NPs (Fig. 6d) [21], suggesting that the separation efficiency of the photoinduced electrons and holes is improved through the electronic interaction between graphene and TiO$_2$. Moreover, the core–shell compound also presents strong photocurrent response under visible light (> 420 nm) irradiation, confirming high photo-activity. The photocurrent enhancement is also observed in other CSSG compounds [36, 65,

89], which may benefit from the large internal electrical field building at the interface of the semiconductors and graphene and the high mobility of carriers in the graphene. Bera et al. found that the photocurrent density of ZnO/G core–shell hollow microspheres (CSHM) is higher than that of pristine ZnO CSHM as well as other ZnO/G nanocomposites (solid MSs and hollow MSs) [65], which may originate from the superior light scattering ability, high surface area, and more active sites for electron conduction. Moreover, for pristine ZnO, the poor stability of photocurrent is found with continuous decay on prolonging the irradiation time due to the consumption of photogenerated holes as a result of self-oxidation of ZnO with existing oxygen atom on the ZnO surface, whereas the existence of graphene layers on ZnO NPs in ZnO/G CSHM offers a sufficient transport pathway of the photogenerated electrons in the system that enhances photostability for the direct chemical contact and charge transfer between ZnO and graphene. Shao et al. discovered that the core–shell ZnO/G NPs show a fast photoresponse under the chopped UV light, with rising and falling edges of the transient response in the time span of 9 and 11 ms, respectively [38], suggesting potential application on photodetectors. In CdS/G QDs, Zubair et al. found that the photocurrent density increases as the graphene layer thickness increases up to 4.45 mA cm^{-2} by the CdS-0.15G sample. Further increase in the graphene content results in a decrease in photocurrent density for the formation of a thicker graphene layer which hinders light absorption in CdS [80]. The result suggests an optimal thickness of the graphene shell in the CSSG nanomaterials for the high performance. Bu et al. found that the photocurrent density of ZnO/G decreases with increasing cycles of white light switching on and off [71], indicating the existence of corrosion of ZnO during the tests, which could be due to the photoelectrochemical reactions.

Instead of the stable photocurrent, a continuous decrease or increase in the photocurrent may be observed upon on-and-off switching of the light irradiation, as shown in Fig. 6e, f [58]. For the core–shell perylene diimide/rGO NWs, the declining photocurrent in light is related to the existence of depletion heterojunction layer and metastable electronic states in the bandgap, and the rapid photocurrent saturation via the rGO shell, while the enhancing photocurrent in dark is due to the synergistic interaction of the efficient exciton dissociation and more rapid charge transport via the rGO shell.

5 Photocatalytic Applications

Due to the special architecture and large interfacial area, the CSSG nanomaterials can increase specific surface area, extend light absorption range, maximize light utilization, reduce electric resistance, enhance charge separation and conduction for the built-in electric field at the interfacial junction, reinforce flexibility and mechanical properties, and stabilize the structure of the core material, thus having broad applications in photocatalysis [50, 73, 96], photodetector [38], phototransistor [58], light-emitting diode (LED) [49, 98], solar cell [47, 74], lithium-ion battery (LIB) [40, 68, 91], supercapacitor [60, 71, 93], gas sensor [45, 75, 92], interfacial bonding [76, 81], filtration membrane [46], adsorber [88], and so on. The photocatalysis is widely used in energy conversion and environmental remedy. The single semiconductor materials often have low catalytic efficiency for the poor utilization of solar energy and rapid recombination of photogenerated electron–hole pairs. The emergence of CSSG nanoarchitectures provides new ideas to address these issues. In this section, the CSSG nanomaterials acting as photocatalysts will be discussed in detail, which will focus on the pollutant degradation, hydrogen generation, and carbon dioxide reduction. The parameters influencing the photocatalytic performance will be elucidated, and possible mechanisms for the enhanced photocatalytic performance will be analyzed based on the electric band alignment and charge transport of the CSSG photocatalysts.

5.1 Degradation of Organic Pollutants

In terms of degrading organic pollutants, photocatalysis is a relatively economical and environmentally friendly method. By constructing a core–shell structure of semiconductor-graphene materials, strong oxidizing holes and reductive electrons are generated during the light irradiation, which can produce active radicals, such as hydroxyl radicals ($\cdot$OH), superoxide radicals ($\bullet O_2^-$), and holes, for the decomposition of most organic pollutants into carbon dioxide, water, and other harmless compounds [3, 112, 113]. Bu et al. successfully removed rhodamine B (RhB) from aqueous solution using ZnO/G NPs as the catalyst [71]. The RhB dye was degraded completely in 20 min under white light (Fig. 7a). The photocatalytic activity of the specimen

was significantly enhanced, with onefold improvement by the Ag modification. He et al. synthesized $SrTiO_3$/G NPs as the catalyst [36]. The RhB was degraded under UV light, and the photocatalytic performance of the specimen was modulated by the shell thickness (Fig. 7b). The composite in an optimal shell thickness showed significantly enhanced photocatalytic activity compared with the $SrTiO_3$, which was attributed to the special core–shell structure and chemical bond (Ti-C) for rapid interfacial electron transfer and effective electron–hole separation. The catalytic activity of the $SrTiO_3$-based powders can be described by the pseudo-first-order kinetics model in Fig. 7c, which is also applied to other semiconductor materials [54, 114]. The size effect of the shell layer on the photocatalytic performance is also observed in other CSSG materials. For the SiC/G NPs, the optimal layer number of the G shell is 4–9 (Fig. 7d, e) [19]. Moreover, the core size also plays a vital role in the catalytic activity. As shown in Fig. 7f [19], the smaller size of the SiC core, the better photocatalytic performance of the SiC/G NPs, which may result from the large surface area of the small particles for the absorption and degradation of the dye molecules. Zhang et al. grew G-wrapped rose-like $Bi_2O_2CO_3$ (WBGR) core–shell structure to maximize contact area and quantum efficiency [37]. The WBGR displayed the highest apparent rate constant (2.81×10^{-4} s^{-1}) for carbamazepine degradation, which was 8.67 and 4.15 times higher than that of $Bi_2O_2CO_3$ and mixed graphene-$Bi_2O_2CO_3$ (BGR), respectively (Fig. 7g). The G shell encapsulation not only inhibited aggregation of the $Bi_2O_2CO_3$ MSs but also protected them from structural destruction. The core–shell structures could promote photoexcited electron transfer from $Bi_2O_2CO_3$ to G by the formation of C-Bi bonds. Preetha et al. found that the boron doping in the graphene layer can significantly improve photocatalytic performance of the core–shell $SrFeO_3$/B-rGO NSs (Fig. 7h) [89], due to the enhanced electronic and transport properties while lowering resistivity. Besides the doping in the graphene layer, the ionic doping in the semiconductor cores, the introduction of vacancies, noble metal NPs and narrow bandgap semiconductors can also enhance photocatalytic activity of the CSSG materials. Furthermore, some additives in the organic solution can speed up the degradation. As shown in Fig. 7i [69], the hydrogen peroxide (H_2O_2) in the methylene blue (MB) solution accelerated the catalytic performance of the core–shell MoS_2/G nanocomposite as the photoinduced electrons were immediately captured by the H_2O_2 to produce hydroxyl radicals.
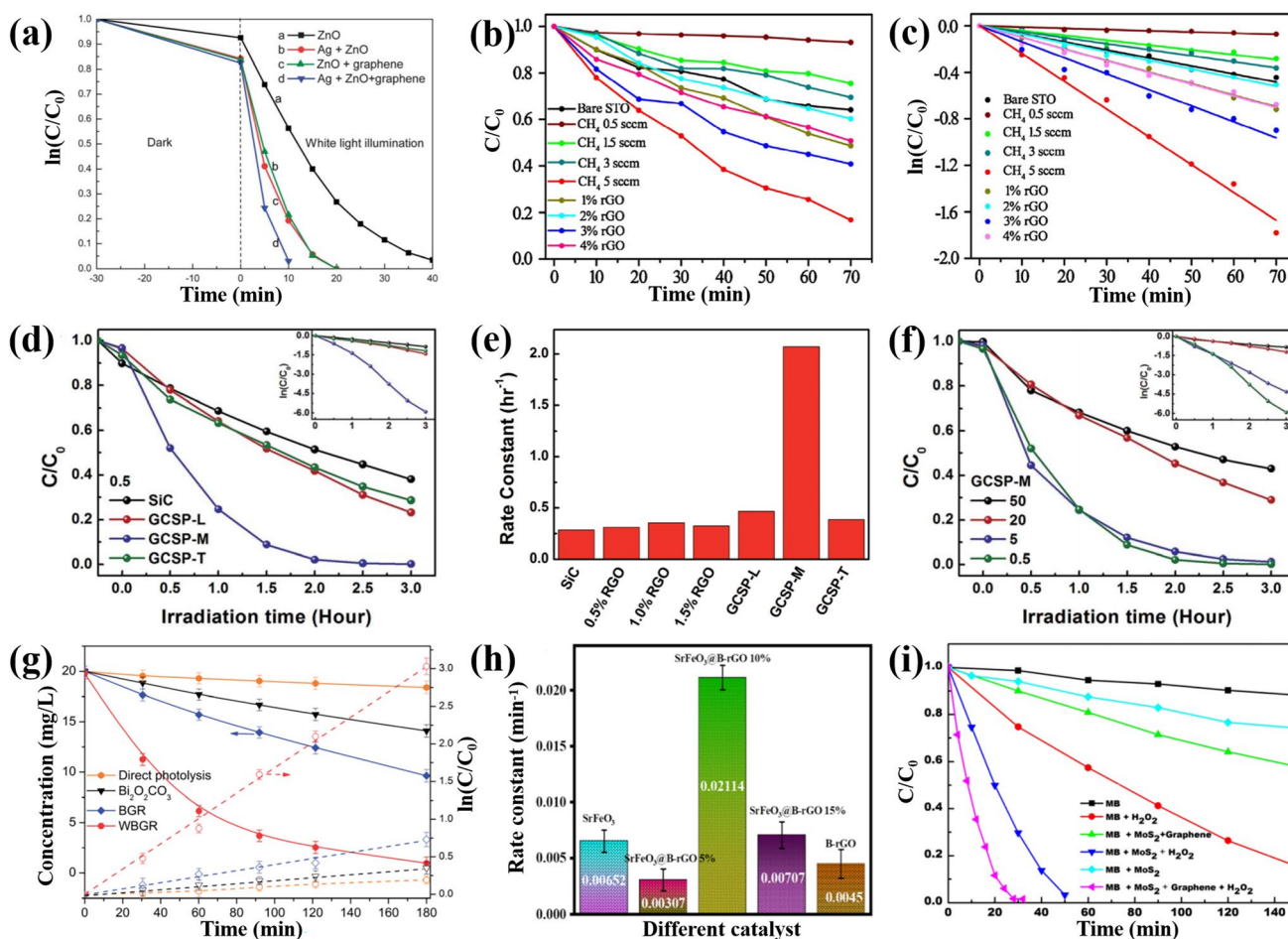
Fig. 7 Photocatalytic activity of the CSSG materials and their pristine semiconductors: **a** Time profiles of RhB degradation in the presence of the ZnO, ZnO/Ag. ZnO/G. ZnO/G/Ag under white light illumination (reproduced with permission from Ref. [71]. Copyright 2013 RSC Publishing). **b** Time profiles of RhB degradation in the presence of $SrTiO_3$ NPs and core–shell $SrTiO_3$/G NPs in different growing conditions under UV light irradiation. **c** Pseudo-first-order fitting results of the RhB degradation in the presence of $SrTiO_3$ NPs and core–shell $SrTiO_3$/G NPs (reproduced with permission from Ref. [36]. Copyright 2017 Elsevier Publishing). **d** Time profiles of RhB photodegradation in the presence of SiC/G NPs (GCSP) covered with different graphene thicknesses together with pristine SiC powder in sizes of 0.5 mm. The inset is the natural logarithm curves corresponding to the concentration ratio, where the unit of abscissa is hour. **e** Degradation rate constants of RhB in the presence of 0.5 mm pristine SiC, corresponding rGO/SiC composites and GCSP, respectively. **f** Time profiles of RhB photodegradation in the presence of GCSP with the optimal graphene thickness in the four sizes. The inset is the natural logarithm curves corresponding to the concentration ratio, where the unit of abscissa is hour (reproduced with permission from Ref. [19]. Copyright 2014 RSC Publishing). **g** Time profiles of carbamazepine photodegradation in the presence of $Bi_2O_2CO_3$, graphene–$Bi_2O_2CO_3$ (BGR), and graphene-wrapped rose-like $Bi_2O_2CO_3$ (WBGR) (solid lines) (reproduced with permission from Ref. [37]. Copyright 2014 RSC Publishing), and the apparent pseudo-first-order rate constant (dashed lines). **h** Kinetic constants of tetracycline photodegradation in the presence of $SrFeO_3$, B-rGO, $SrFeO_3$/B-rGO in different shell contents (reproduced with permission from Ref. [89]. Copyright 2023 ACS Publishing). **i** Time profiles of MB degradation containing different catalysts (reproduced with permission from Ref. [69]. Copyright 2017 Elsevier Publishing)

The photocatalytic efficiency and kinetic constant of some typical CSSG nanomaterials are supplied in Table 3 for comparison [115–123]. It is found that the photocatalytic activity of the CSSG nanomaterials is modulated by the components, structure, additives, incident light wavelength, and intensity. The catalytic effect varies for different pollutants due to the different organic components and structure. The coating layer obviously enhances the photocatalytic activity. The kinetic constant of the CSSG materials with the G shell is usually larger than that with rGO or GO shell, which may result from the improved electron conduction and compact coverage of the G sheets.

Based on the band alignment of heterogeneous components and experimental characterizations, possible

Table 3 Comparison of photocatalytic activity of some typical CSSG nanomaterials and their pristine semiconductors for degradation of organic contaminants in aqueous solutions

Materials	Light source	Pollutant	Photocatalytic efficiency	Kinetic constant (min^{-1})	References
$SrTiO_3$ NPs	Mercury 350 W, 5 mW cm^{-2}	Rhodamine B	3% in 70 min	0.0068	[36]
$SrTiO_3$/G NPs	Mercury 350 W, 5 mW cm^{-2}	Rhodamine B	85% in 70 min	0.0239	
$SrTiO_3$/rGO NPs	Mercury 350 W, 5 mW cm^{-2}	Rhodamine B	55% in 70 min	0.0137	
MoS_2 nanosheets	Xenon 500 W, distance 10 cm	Methylene blue (adding H_2O_2)	68% in 28 min	0.065	[69]
MoS_2/G nanosheets	Xenon 500 W, distance 10 cm	Methylene blue (adding H_2O_2)	99% in 28 min	0.138	
SiC NPs	Mercury 500 W, 1 mW cm^{-2}	Rhodamine B	~55% in 120 min	~0.0058	[19]
SiC/G NPs	Mercury 500 W, 1 mW cm^{-2}	Rhodamine B	~100% in 120 min	~0.0333	
ZnO NPs	Xenon 300 W, distance 10 cm	Rhodamine B	100% in 40 min	–	[71]
ZnO/G NPs	Xenon 300 W, distance 10 cm	Rhodamine B	100% in 20 min	–	
ZnO/G/Ag NPs	Xenon 300 W, distance 10 cm	Rhodamine B	100% in 10 min	–	
ZnO NFs	UV lamp 24 W	Methylene blue	24% in 120 min	–	[56]
ZnO/GO NFs	UV lamp 24 W	Methylene blue	~97% in 120 min	–	
ZnO core–shell hollow MSs	Xenon 300 W	Rhodamine B	~70% in 100 min	0.012	[65]
ZnO/G hollow MSs	Xenon 300 W	Rhodamine B	~100% in 100 min	0.049	
ZnO/G core–shell hollow MSs	Xenon 300 W	Rhodamine B	~100% in 100 min	0.051	
ZnO/Co_3O_4 NPs	Phillips visible lamps 300 W	2,4-dichlorophenol	~55% in 150 min	0.017	[115]
ZnO/Co_3O_4/G NPs	Phillips visible lamps 300 W	2,4-dichlorophenol	91% in 150 min	0.0338	
ZnS QDs	LED 60 W	Diazinon	~23% in 30 min	0.019	[94]
	LED 60 W	Fenitrothion	~30% in 30 min	0.022	
ZnS/S-G QDs	LED 60 W	Diazinon	~40% in 30 min	0.029	
	LED 60 W	Fenitrothion	~43% in 30 min	0.031	
ZnS/S-G QDs/Ag_2S	LED 60 W	Diazinon	>99% in 60 min	0.053	
	LED 60 W	Fenitrothion	>99% in 60 min	0.056	
$Bi_2O_2CO_3$ nanoflowers	Xenon 300 W	Carbamazepine	29.6% in 180 min	0.0207	[37]
$Bi_2O_2CO_3$/G nanoflowers	Xenon 300 W	Carbamazepine	95.4% in 180 min	0.1686	
TiO_2 NPs	Xenon 450 W	Methylene blue	~10% in 60 min	0.00328	[21]
TiO_2/G NPs	Xenon 450 W	Methylene blue	~90% in 60 min	0.0341	
TiO_2 NPs	UV lamp 2×15 W	Rhodamine B	~75% in 240 min	–	[79]
TiO_2/G NPs	UV lamp 2×15 W	Rhodamine B	~100% in 240 min	–	
TiO_2 MSs	Xenon 500 W	Rhodamine B	~50% in 105 min	–	[116]
TiO_2/GO MSs	Xenon 500 W	Rhodamine B	100% in 130 min	–	
TiO_2 MSs	Mercury 500 W	Rhodamine B	~95% in 105 min	–	
TiO_2/GO MSs	Mercury 500 W	Rhodamine B	100% in 25 min	–	
TiO_2 NSs	Xenon 500 W	Methyl orange	~55% in 150 min	0.00533	[117]
TiO_2/Au NSs	Xenon 500 W	Methyl orange	~58% in 150 min	0.00593	
TiO_2/rGO NSs	Xenon 500 W	Methyl orange	~78% in 150 min	0.0104	
TiO_2/Au/rGO NSs	Xenon 500 W	Methyl orange	~93% in 150 min	0.0168	
TiO_2 NSs	Germicidal lamp 15 W	Methyl orange	~34% in 50 min	0.00837	
TiO_2/Au NSs	Germicidal lamp 15 W	Methyl orange	~52% in 50 min	0.0147	
TiO_2/rGO NSs	Germicidal lamp 15 W	Methyl orange	~63% in 50 min	0.0182	
TiO_2/Au/rGO NSs	Germicidal lamp 15 W	Methyl orange	~91% in 50 min	0.0479	

Table 3 (continued)

Materials	Light source	Pollutant	Photocatalytic efficiency	Kinetic constant (min^{-1})	References
TiO$_2$ NWs	Mercury 500 W, 138.2 mW cm^{-2}	Methylene blue	74.3% in 60 min	–	[50]
TiO$_2$/rGO NWs	Mercury 500 W, 138.2 mW cm^{-2}	Methylene blue	91.6% in 60 min	–	
rGO/TiO$_2$ NSs	Metal halide 400 W cutoff filter (> 400 nm)	Rhodamine B	~78% in 100 min	0.01475	[118]
Au/TiO$_2$ NSs	Metal halide 400 W cutoff filter (> 400 nm)	Rhodamine B	~85% in 100 min	0.01801	
Au/rGO/TiO$_2$ NSs	Metal halide 400 W cutoff filter (> 400 nm)	Rhodamine B	~99% in 100 min	0.02749	
rGO/TiO$_2$ NSs	Xenon 350 W	Rhodamine B	~90% in 100 min	0.04618	
Au/TiO$_2$ NSs	Xenon 350 W	Rhodamine B	~90% in 100 min	0.05242	
Au/rGO/TiO$_2$ NSs	Xenon 350 W	Rhodamine B	99.6% in 50 min	0.09715	
TiO$_2$ hollow NSs	Mercury 500 W	Rhodamine B	80.2% in 210 min	0.0473	[67]
TiO$_2$/rGO hollow NSs	Mercury 500 W	Rhodamine B	95.2% in 210 min	0.1224	
TiO$_2$ hollow NSs	Xenon 500 W	Rhodamine B	54.0% in 210 min	0.0027	
TiO$_2$/rGO hollow NSs	Xenon 500 W	Rhodamine B	91.8% in 210 min	0.0094	
GO/TiO$_2$ MSs on electrospun polymer fibrous membrane	Xenon 500 W	Methylene blue (adding H$_2$O$_2$)	90.8% in 60 min	–	[46]
	Xenon 500 W	Crystal violet (adding H$_2$O$_2$)	92.5% in 60 min	–	
	Xenon 500 W	Methyl orange (adding H$_2$O$_2$)	85.4% in 60 min	–	
	Xenon 500 W	Congo red (adding H$_2$O$_2$)	72.0% in 60 min	–	
SnO$_2$ MSs	Mercury 500 W	Methyl orange	~50% in 60 min	0.010	[119]
SnO$_2$/rGO MSs (by chemical bonding)	Mercury 500 W	Methyl orange	~92% in 60 min	0.038	
SnO$_2$/rGO MSs (by electrostatic interaction)	Mercury 500 W	Methyl orange	~73% in 60 min	0.021	
SrFeO$_3$ NSs	Xenon 300 W	Tetracycline	39% in 75 min	0.0065	[89]
SrFeO$_3$/B-rGO NSs	Xenon 300 W	Tetracycline	92.4% in 75 min	0.0211	
Fe$_2$O$_3$ NPs	Xenon 300 W	Cephalexin	40% in 60 min	–	[120]
Fe$_2$O$_3$@N-G NPs	Xenon 300 W	Cephalexin	90% in 60 min	–	
Fe$_3$O$_4$/MIL-100(Fe) MSs	Xenon 500 W	2,4-dichlorophenol (adding H$_2$O$_2$)	93.5% in 40 min	0.1439	[121]
Fe$_3$O$_4$/GO/MIL-100(Fe) MSs	Xenon 500 W	2,4-dichlorophenol (adding H$_2$O$_2$)	100% in 40 min	0.1969	
g-C$_3$N$_4$ nanosheets	Xenon 300 W, cutoff filter (< 420 nm) distance 15 cm	Doxycycline	~57% in 50 min	0.01632	[122]
Ag$_2$CrO$_4$ NPs	Xenon 300 W, cutoff filter (< 420 nm) distance 15 cm	Doxycycline	~62% in 50 min	0.01852	
Ag$_2$CrO$_4$/g-C$_3$N$_4$ NPs	Xenon 300 W, cutoff filter (< 420 nm) distance 15 cm	Doxycycline	~85% in 50 min	0.03568	
Ag$_2$CrO$_4$/N-G QDs/g-C$_3$N$_4$ NPs	Xenon 300 W, cutoff filter (< 420 nm) distance 15 cm	Doxycycline	~100% in 50 min	0.08839	
g-C$_3$N$_4$ nanosheets	Xenon 300 W, cutoff filter (> 420 nm) distance 15 cm	Doxycycline	~45% in 80 min	0.00705	
Ag$_2$CrO$_4$ NPs	Xenon 300 W, cutoff filter (> 420 nm) distance 15 cm	Doxycycline	~55% in 80 min	0.00962	

Table 3 (continued)

Materials	Light source	Pollutant	Photocatalytic efficiency	Kinetic constant (min^{-1})	References
Ag$_2$CrO$_4$/g-C$_3$N$_4$ NPs	Xenon 300 W, cutoff filter (> 420 nm) distance 15 cm	Doxycycline	~88% in 80 min	0.0263	
Ag$_2$CrO$_4$/N-G QDs/g-C$_3$N$_4$ NPs	Xenon 300 W, cutoff filter (> 420 nm) distance 15 cm	Doxycycline	~100% in 60 min	0.04052	
BiOBr nanosheets	Neon tube, 8 mW cm^{-2}	Orange II	55% in 105 min	~0.033	[123]
BiOBr/rGO nanosheets	Neon tube, 8 mW cm^{-2}	Orange II	97% in 90 min	0.040	
BiOBr nanosheets	Hg/Xe lamp, 20 mW cm^{-2}	Acetaminophen	55% in 105 min	0.003	
BiOBr/rGO nanosheets	Hg/Xe lamp, 20 mW cm^{-2}	Acetaminophen	93% in 105 min	0.006	

mechanisms for enhanced photocatalytic performance of the CSSG photocatalysts have been proposed. In the core–shell SiC/G (Fig. 8a) [19], the electrons are excited from the valence band (VB) to conduction band (CB) of SiC particles by the UV light, which transfer to the graphene shell rapidly for the high carrier transport mobility, and then are captured by oxygen in solution to produce active oxygen species. The RhB is decomposed either by the free holes in the SiC through the defect sites of graphene or by the active oxygen species. The transfer of the photoinduced electrons from the semiconductor core to the graphene shell is also proposed in MoS$_2$/G [69], BiOBr/rGO [123], Fe$_2$O$_3$/N-G [120], and other CSSG catalysts. In the core–shell TiO$_2$/G NPs, the intra-bandgap energy level of TiO$_2$ is narrowed from 3.2 to 2.8 eV by direct interaction with Ti atoms and C atoms during the synthesis of graphene-TiO$_2$ NPs (Fig. 8b) [21]. Under illustration of the visible light, the electrons are excited from the highest occupied molecular orbital (HOMO) level to lowest unoccupied molecular orbital (LUMO) level of the MB molecules, which transfer to the CB of TiO$_2$ by the conductive graphene layer. The valence electrons of TiO$_2$ are also excited to the CB by absorbing incident light. The electrons in the CB can be trapped by oxygen molecules in the aqueous solution to form reactive oxygen species that cause the oxidative decomposition of MB molecules. The holes in the VB of the semiconductor may also participate in the pollutant degradation. This pattern resembles that in the Bi$_2$O$_2$CO$_3$/G compound [37]. In the SrFeO$_3$/B-rGO NSs, the surface potential promotes effective interaction between the pollutant and the catalyst. Additionally, the heterojunction forms a type-II band alignment, as shown in Fig. 8c [89], which facilitates the transport of the photoinduced electrons in the CB of B-rGO to the CB of SrFeO$_3$, while the residual holes in the VB of SrFeO$_3$ to the VB of B-rGO. The

collecting electron in the CB of SrFeO$_3$ will interact with O$_2$ to form superoxide radicals, while the holes react with H$_2$O to generate hydroxy radicals, and both of the radicals induce decomposition of the TC molecules. The enhanced charge separation and photocatalytic activity for the type-II band alignment are also observed in SnO/rGO compound [119], while in the core–shell structured TiO$_2$/Au/rGO ternary photocatalyst, the promoted photocatalytic performance is attributed to the synergistic effect between Au NPs, TiO$_2$ and rGO, and the existence of multi-channel electron transfer paths [117]. As shown in Fig. 8d, under UV light irradiation, the photoinduced electrons in the CB of TiO$_2$ transfer to the neighboring rGO sheets directly or to the adjacent Au NPs first and then further migrate to the rGO sheets, which react with resolved oxygen nearby to generate superoxide radicals for the MO degradation, while the left holes in the VB band of TiO$_2$ decompose MO. Under visible light, the electron–hole pairs in the TiO$_2$ cannot be separated for low photon energy, but they can be generated in surface of the Au NPs for the surface plasmon resonance. These electrons also transport to the rGO sheets in the two paths for the MO degradation. The remaining holes in the Au NPs act as those in the VB of TiO$_2$.

In fact, except the catalytic properties, the photocatalytic activity of the CSSG materials is also influenced by the environment, such as pH value (Fig. 9a) and temperature (Fig. 9b) of the solution [89, 94]. Furthermore, to be a widespread photocatalyst, the stability and reusability of the catalyst are essential. The recycling experiment indicates that the photocatalytic efficiency of ZnO/GO core–shell NFs (CSNF) keeps stable in the three cycles, while that of ZnO NFs and the blend of ZnO NFs and GO powder decreases from 76 to 68% and 68% to 55%, respectively, between the first and third cycles (Fig. 9c) [56], indicating that the coating layer
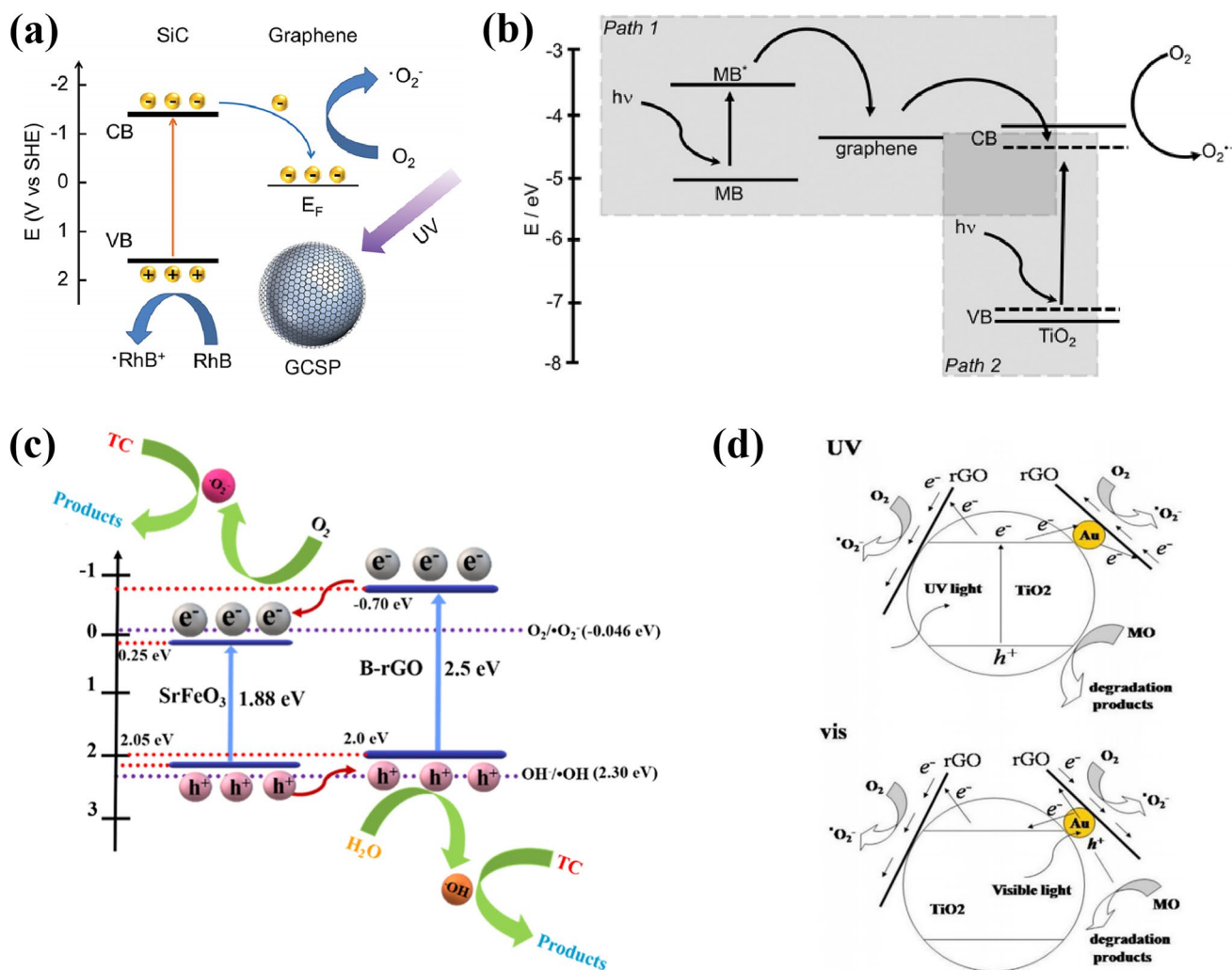
Fig. 8 Possible enhancement mechanisms of photocatalytic performance over different CSSG catalysts: **a** SiC/G NPs (reproduced with permission from Ref. [19]. Copyright 2014 RSC Publishing). **b** TiO$_2$/G NPs (reproduced with permission from Ref. [21]. Copyright 2012 WILEY–VCH Publishing). **c** SrFeO$_3$/B-rGO nanocomposites (reproduced with permission from Ref. [89]. Copyright 2023 ACS Publishing). **d** TiO$_2$/Au/rGO NPs (reproduced with permission from Ref. [117]. Copyright 2017 Elsevier Publishing)

can eliminate or reduce the photo-corrosion effect of the ZnO core. The improved recyclability for the compacted coating layer is also observed in other CSSG catalysts. The mineralization efficiency of the organic pollutants can be detected by the total organic carbon (TOC) concentration. As shown in Fig. 9d [89], the TOC removal reaches 38% after 75 min illumination, which suggests that the core–shell SrFeO$_3$/B-rGO NSs are able to degrade TC efficiently. However, the mineralization efficiency is generally lower than the degradation efficiency for the formation of certain organic intermediates. In order to verify the reactive species in the photodegradation process, the radical trapping can be conducted on the catalyst in the organic solution. Various

scavengers, such as isopropyl alcohol (IPA) or tert-butyl alcohol (TBA) for the hydroxyl radicals, ethylenediamine tetraacetic acid (EDTA) or ammonium oxalate (AO) for the holes, AgNO$_3$ for the electrons, and 1,4-benzoquinone (BQ) for the superoxide radicals, can be employed for the radical trapping experiment. As shown in Fig. 9e [89], the reduced efficiency in the present of IPA, EDTA, and BQ indicates that the three radicals are all involved in the degradation performance. The significant reduction in the present of BQ reveals the major role of superoxide radicals in the degradation process. The electron paramagnetic resonance (EPR) can be used to detect the radicals. The characteristic peaks of 5,5-dimethyl-1-pyrroline-N-oxide (DMPO)-•O$_2^-$ and
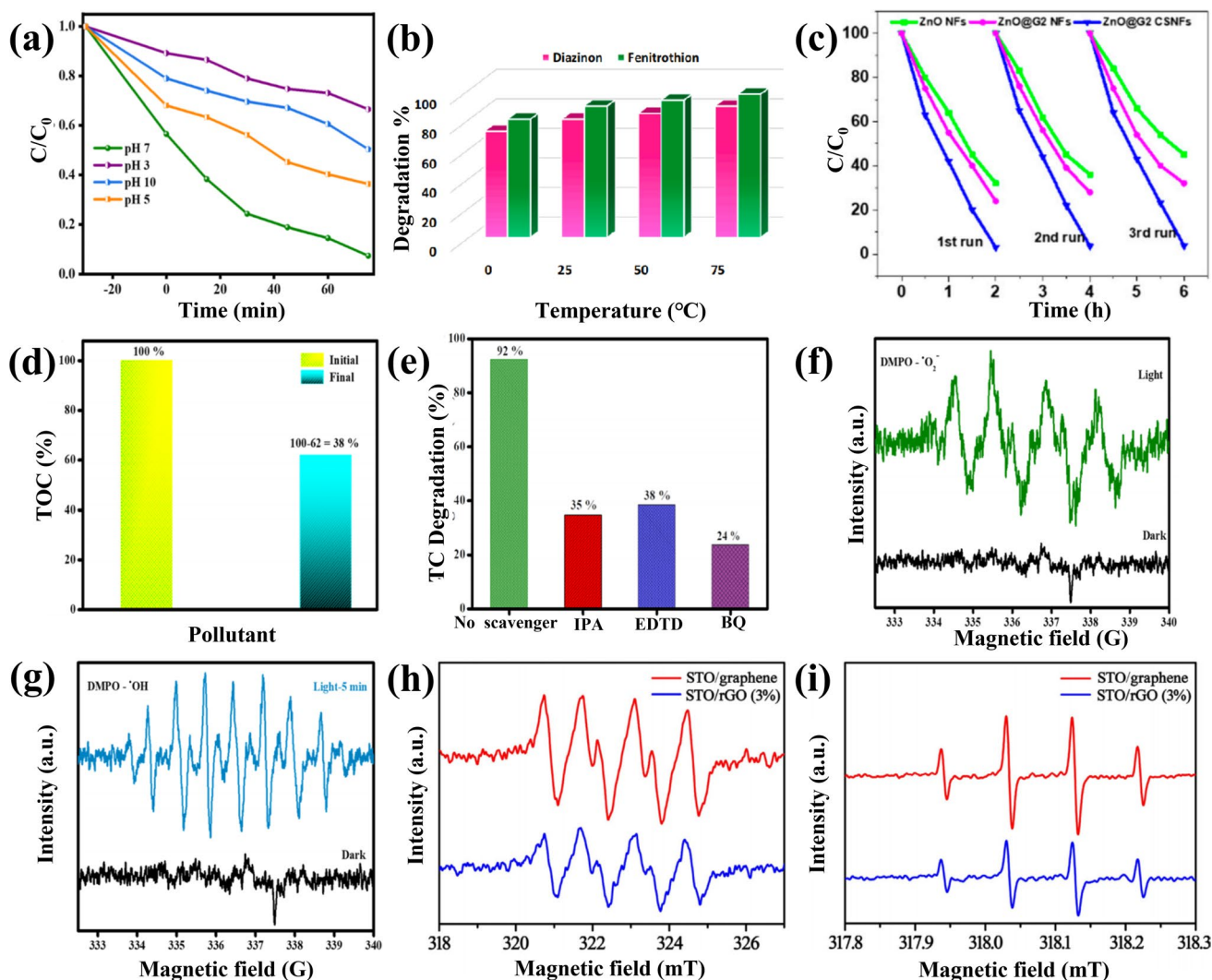
Fig. 9 Environmental parameters, mineralization efficiency, radical trapping and detection in the photocatalytic performance of CSSG catalysts: **a** Influence of pH on the photocatalytic degradation of tetracycline in the presence of $SrFeO_3$/B-rGO NSs (reproduced with permission from Ref. [89]. Copyright 2023 ACS Publishing). **b** Influence of temperature on the photocatalytic degradation of diazinon and fenitrothion in the presence of ZnS/S-G/Ag_2S NPs (reproduced with permission from Ref. [94]. Copyright 2022 Elsevier Publishing). **c** Photocatalytic degradation cycles of ZnO NFs, ZnO NF mixed with GO (ZnO@G2 NFs), and core–shell ZnO/GO NFs (ZnO@G2 CSNFs) (reproduced with permission from Ref. [56]. Copyright 2020 MDPI Publishing). **d** TOC analysis of the degraded tetracycline in the presence of $SrFeO_3$/B-rGO. **e** Scavenger test of the degraded tetracycline in the presence of $SrFeO_3$/B-rGO. **f** EPR analysis of DMPO- in the presence of $SrFeO_3$/B-rGO. **g** EPR analysis of DMPO-·OH in the presence of $SrFeO_3$/B-rGO (reproduced with permission from Ref. [89]. Copyright 2023 ACS Publishing). **h** EPR analysis of DMPO- in the presence of $SrTiO_3$/G and $SrTiO_3$/rGO. **i** EPR analysis of DMPO-·OH in the presence of $SrTiO_3$/G and $SrTiO_3$/rGO (reproduced with permission from Ref. [36]. Copyright 2017 Elsevier Publishing)

DMPO-·OH in Fig. 9f, g indicate that the active radicals can be only produced under light irradiation [89]. The stronger intensity of the EPR signature in Fig. 9h, i for $SrTiO_3$/G than $SrTiO_3$/rGO represents more active ·OH and •O_2^- radicals produced by the incident photons [36], leading to the higher photocatalytic activity.

5.2 Generation of Hydrogen Gas

Photocatalytic hydrogen production is one of the effective means to solve energy problems. The hydrogen gas (H_2) can be produced from the massive water on earth. To generate H_2 from water by the photocatalysis, the redox potentials of the catalysts should straddle the reduction potential of the

H$^+$/H$_2$ redox pair (0 V under the normal hydrogen electrode, NHE) and the oxidation potential of the O$_2$/H$_2$O redox pair (1.23 V) [4, 6], which requires the bandgap of a semiconductor catalyst at least 1.23 eV and the wavelength of the incident light about 1008 nm or shorter. Some semiconductors with narrow bandgap meet the condition, but they are generally suffering rapid electron–hole pair recombination and photocorrection, while for the wide-bandgap semiconductors, the oxidation potentials are usually far more positive than 1.23 V, leading to the limited solar spectrum in the UV range. Therefore, the band engineering of the semiconductor catalysts becomes crucial for an efficient performance. Zubair et al. prepared core–shell particles of C-doped CdS and graphene for photocatalytic reduction of H$_2$ [80]. The most active CdS/G (CdS-0.15G) NPs produced 3.12 mmol g^{-1} h^{-1} of H$_2$ under simulated solar light (Fig. 10a), which was ~ 4.6 times superior than the pure CdS NPs, giving an apparent quantum efficiency of 11.7%. In this sample, the C doping induced the bandgap narrowing of the CdS from 2.32 to 2.24 eV, which increased the light absorption range. The photoinduced electrons in the CB of CdS transferred to graphene layer immediately for its favorable work function and then reduced H$^+$ in the water to generate H$_2$. The holes in the VB of CdS were also extracted by the graphene layer and neutralized by the hole scavengers in the solution to maintain the charge balance (Fig. 10b) [80]. Lu et al. prepared graphene-covered SiC particles (GCSPs) by thermal decomposition and used them as the catalyst [96]. The optimized sample achieved a high hydrogen evolution rate of 472.4 μmol g^{-1} h^{-1} in xenom light (Fig. 10c). Its photocatalytic activity exceeded the corresponding activity observed on pristine SiC particles by more than 33 times and that observed on Pt decorated SiC particles by more than 4 times, confirming superior functionality of the graphene as a cocatalyst than the noble metals. In this core–shell heterojunction, opposite charge doping (bipolar charge) regions coexisted in the graphene shell for a series of continuous facets on the SiC surface. Therefore, two inverse energy band configurations of the Schottky junction were created between the graphene and SiC, which served as the charge transfer channels for the built-in potential and the Schottky barrier (Fig. 10d) [96], leading to the efficient photocatalytic hydrogen evolution. Except for a single semiconductor component, the combination of the graphene with two or more semiconductor components in a core–shell structure may be facile and effective to extend light response, separate electron–hole

pairs, and improve hydrogen generation. For instance, Gao et al. combined tungsten nitride quantum dots encapsulated in graphene (WN@C) with semiconductor ZnIn$_2$S$_4$ [124]. The hydrogen evolution activity of the optimal sample reached 196.0 μmol g^{-1} h^{-1}, exhibiting 61 times larger than that of ZnIn$_2$S$_4$ and 12 times than that of WN@C under the visible light (Fig. 10e). The enhanced activity was attributed to the lower overpotential of hydrogen evolution reaction, the reduced apparent activation energy, the decreased Gibbs free energy of H adsorption, and the inhibited recombination of photo-charges for the Z-scheme band alignment of the heterojunction in Fig. 10f [124].

For comparison, the photocatalytic activities of some typical CSSG nanomaterials and their pristine semiconductors are listed in Table 4 [124–130]. It is found that the photocatalytic performance of the CSSG materials is much better than that of the pristine semiconductor. The hydrogen evolution rate of the semiconductor can be improved several to dozens of times for the combination of the conductive graphene sheets. The special core–shell structure and synergistic interaction between the core and the shell can greatly improve the electric conductivity, facilitate the mass/ion transport and gas emissions, and expose more active sites for the reactant adsorption. The structural defects and functional groups in the graphene of the CSSG materials can also increase the adsorption equilibrium thermodynamically and promote the substrate-assisted desorption pathway kinetically [131, 132] and thus lead to the enhancement of catalytic activity and long-term stability of the catalysts for overall water splitting. Secondly, the catalysts, including the single semiconductor and the CSSG material, with a narrower bandgap own a more active photocatalytic performance. For example, the bandgap of CdS (2.40 eV) is smaller than that of SiC (3.26 eV), but the hydrogen evolution rate of the former (670 μmol g^{-1} h^{-1}) is much larger than that of the latter (30 μmol g^{-1} h^{-1}) [69, 80]. The effect may be due to the more photoinduced charges for the extended and enhanced light excitation. However, for the hydrogen production, the redox potentials of the catalyst should keep straddling the reduction potential of the H$^+$/H$_2$ redox pair and the oxidation potential of the O$_2$/H$_2$O redox pair. Thirdly, except for the graphene, incorporating two or more semiconductor and other components in the CSSG nanomaterials can drastically improve the photocatalytic activity, which may benefit from the different light response of the different component and
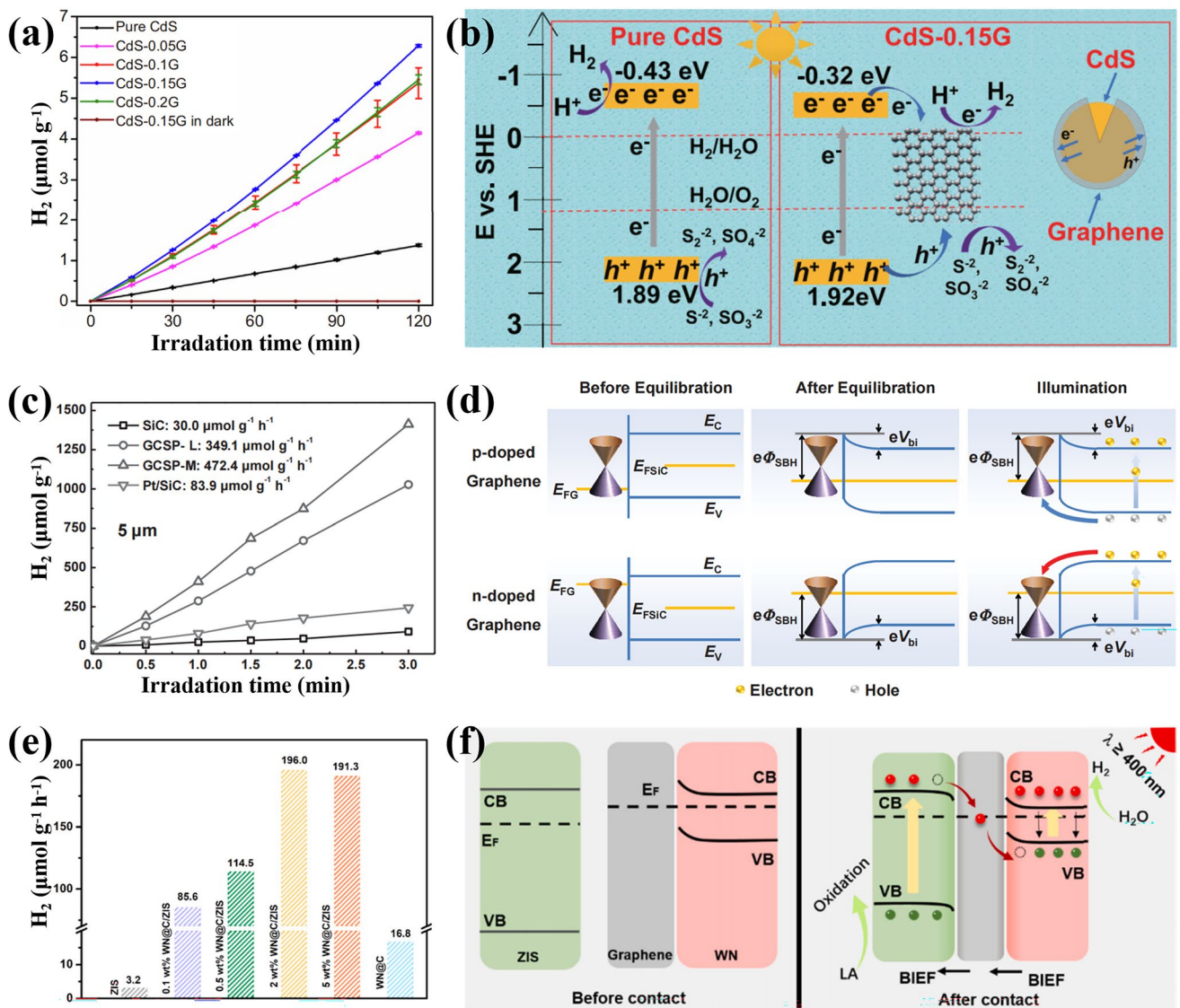
Fig. 10 Hydrogen (H_2) evolutions as catalyzed by different CSSG materials and their enhancement mechanisms: **a, b** CdS/G (reproduced with permission from Ref. [80]. Copyright 2020 KeAi Publishing). **c, d** SiC/G (reproduced with permission from Ref. [96]. Copyright 2015 WILEY–VCH Publishing). **e, f** WN/G/ZnIn$_2$S$_4$ (reproduced with permission from Ref. [124]. Copyright 2021 Elsevier Publishing)

the effective charge separation and conduction for the built-in potential at the heterojunction.

5.3 Reduction of Carbon Dioxide

The global warming caused by the increasing carbon dioxide (CO_2) in the atmosphere for social production and activities has become one of the greatest crises for human being. Converting CO_2 into renewable fuel by photocatalytic reduction can not only reduce the concentration of CO_2 in air but also relieve the energy shortage, which has achieved much attention as it is economically viable and environmentally friendly. Various semiconductor materials, such as TiO_2, ZnO, CdS, Fe_2O_3, Cu_2O, and WO_3, have been developed as active photocatalysts for CO_2 reduction in the presence of water vapor. However, the limited solar spectrum range and fast recombination of the electron–hole pairs induce low generation rate and apparent quantum efficiency (AQE), and the photogenerated holes may act as strong oxidizing agents for the corrosion of oxide semiconductor [73], leading to the poor stability and recyclability. The construction

Table 4 Comparison of photocatalytic activity of some typical CSSG nanomaterials and their pristine semiconductors for hydrogen generation

Materials	Light source	Sacrificial reagents	Hydrogen evolution rate (μmol g^{-1} h^{-1})	Apparent quantum efficiency (%)	References
SiC NPs	Xenon 300 W, ~50 mW cm^{-2}	None	0	–	[69]
SiC NPs	Xenon 300 W, ~50 mW cm^{-2}	Na$_2$S/Na$_2$SO$_3$	30.0	–	
SiC/G NPs	Xenon 300 W, ~50 mW cm^{-2}	None	33.2	–	
SiC/G NPs	Xenon 300 W, ~50 mW cm^{-2}	Na$_2$S/Na$_2$SO$_3$	472.4	5.6	
WO$_3$-C$_3$N$_4$/G QDs	Xenon 300 W	None	16.8	–	[124]
ZnIn$_2$S$_4$ NPs	Xenon 300 W	None	3.2	–	
WO$_3$-C$_3$N$_4$/G/ZnIn$_2$S$_4$ NPs	Xenon 300 W	None	196.0	–	
Fe$_2$O$_3$/rGO NPs	Xenon 250 W, cutoff filter (> 420 nm)	Triethanolamine	~0	–	[125]
C$_3$N$_4$ nanosheets	Xenon 250 W, cutoff filter (> 420 nm)	Triethanolamine	432.4	–	
C$_3$N$_4$/rGO nanosheets	Xenon 250 W, cutoff filter (> 420 nm)	Triethanolamine	876	–	
Fe$_2$O$_3$/C$_3$N$_4$ NPs	Xenon 250 W, cutoff filter (> 420 nm)	Triethanolamine	~200	–	
Fe$_2$O$_3$/rGO/C$_3$N$_4$ NPs	Xenon 250 W, cutoff filter (> 420 nm)	Triethanolamine	6607	–	
TiO$_2$ NPs	Mercury 125 W and halogen 250 W	PH = 2.5	0	–	[126]
Au-TiO$_2$ NPs	Mercury 125 W and halogen 250 W	PH = 2.5	~160	–	
Au-TiO$_2$/GO NPs	Mercury 125 W and halogen 250 W	PH = 2.5	~456	–	
rGO/TiO$_2$ NSs	Xenon 100 mW cm^{-2}	Methanol	~95	–	[118]
Au/TiO$_2$ NSs	Xenon 100 mW cm^{-2}	Methanol	167	–	
Au/rGO/TiO$_2$ NSs	Xenon 100 mW cm^{-2}	Methanol	309	0.87	
TiO$_2$/G NPs	Xenon 300 W, 150 mW cm^{-2}	Methanol	52.04	~0	[127]
Au/TiO$_2$ NSs	Xenon 300 W, 150 mW cm^{-2}	Methanol	241.63	0.10	
Au/TiO$_2$/G NSs	Xenon 300 W, 150 mW cm^{-2}	Methanol	676.56	0.31	
TiO$_2$ NPs	Xeon solar simulator 150 W, 150 mW cm^{-2}	Na$_2$S/Na$_2$SO$_3$	565	2.16	[128]
CdS NPs	Xeon solar simulator 150 W, 150 mW cm^{-2}	Na$_2$S/Na$_2$SO$_3$	673	2.57	
CdS/TiO$_2$ NPs	Xeon solar simulator 150 W, 150 mW cm^{-2}	Na$_2$S/Na$_2$SO$_3$	954	3.65	
CdS/G/TiO$_2$ NPs	Xeon solar simulator 150 W, 150 mW cm^{-2}	Na$_2$S/Na$_2$SO$_3$	1510	5.78	
CdS NPs	Xenon 150 W, 100 mW cm^{-2}	Na$_2$S/Na$_2$SO$_3$	670	2.7	[80]
C-doped CdS/G NPs	Xenon 150 W, 100 mW cm^{-2}	Na$_2$S/Na$_2$SO$_3$	3120	11.7	
CdS NPs	Xenon 300 W, 100 mW cm^{-2}	Lactic acid	804	1.32	[63]
rGO/CdS nanosheets	Xenon 300 W, 100 mW cm^{-2}	Lactic acid	2880	4.74	
CdS/MoS$_2$ nanosheets	Xenon 300 W, 100 mW cm^{-2}	Lactic acid	5760	9.48	
rGO/CdS/MoS$_2$ nanosheets	Xenon 300 W, 100 mW cm^{-2}	Lactic acid	14,400	23.7	
Cu$_2$O nanocubes	Xenon 300 W, 100 mW cm^{-2}	Methanol	16.8		[129]
Cu$_2$O/Pd nanocubes	Xenon 300 W, 100 mW cm^{-2}	Methanol	32.7		
Cu$_2$O/Pd/rGO nanocubes	Xenon 300 W, 100 mW cm^{-2}	Methanol	123.6		
LaFeO$_3$ NPs	Xenon 300 W	Na$_2$S/Na$_2$SO$_3$	0	–	[130]
N-G nanosheets	Xenon 300 W	Na$_2$S/Na$_2$SO$_3$	340	–	
N-G/Pt NPs	Xenon 300 W	Na$_2$S/Na$_2$SO$_3$	880	–	
LaFeO$_3$/N-G NPs	Xenon 300 W	Na$_2$S/Na$_2$SO$_3$	1860	–	
LaFeO$_3$/N-G/Pt NPs	Xenon 300 W	Na$_2$S/Na$_2$SO$_3$	3520	18.25	

of CSSG may ideally address the issue with the graphene as a conductive and protective layer. Kang et al. fabricated rGO-wrapped Ag/TiO$_2$ NFs for CO$_2$ photoreduction [52]. The sample yielded 4.301 μmol g^{-1} of methane (CH$_4$) in

7 h under visible light, which was 25-fold higher than the bare TiO_2 NFs (Fig. 11a). In this ternary composite, the Ag NPs were inserted between the TiO_2 surface and rGO sheet, which successfully prolonged the spectral reaction from UV to visible region by the LSPR effect. The Schottky barrier at the $Ag-TiO_2$ junction benefited the charge separation, while the rGO layer offered a rapid pathway for trapping electrons from Ag and TiO_2 for its outstanding electron conductivity. The transferred electrons produced an electron-enriched area on the wrapped rGO layer and converted CO_2 to CH_4, while the holes left on the surface of TiO_2 reacted with H_2O to form H^+ and then joined the CO_2 reduction (Fig. 11b) [52]. The NFs showed a consistent CO_2 to CH_4 photoreduction efficiency even after six cycles of testing for 17 h without discernible morphological change. The structural and functional stability for the rigid wrapping of the graphene shell is also observed in other CSSG catalysts, indicating unparalleled advantage of this architecture. The rGO layer as an electron mediator was also applied in the $CdS/rGO/TiO_2$ core–shell nanostructure, but this time it was seated between two semiconductors [73]. The ternary compound made apparent increase of CH_4 evolution compared to CdS, CdS/TiO_2 and CdS/rGO (Fig. 11c). The enhanced photocatalytic performance was attributed to Z-scheme band alignment of the system that the photogenerated electrons from CB of TiO_2 transferred to rGO, and then recombined with existing holes of CdS NSs, allowing that the photogenerated electrons enriched on the CdS semiconductor and holes on TiO_2 for reduction of CO_2 and oxidation of H_2O, respectively (Fig. 11d) [73]. The improved catalytic performance by the band alignment is also observed in other CSSG materials.

Except for the band modification with various components, the enhanced photocatalytic activity of the catalysts can also be achieved by constructing CSSG materials with effective transport channel for the photoinduced charges. For example, Yang et al. fabricated TiO_2 spherical shells with both inner and outer surface modified by graphene [133]. The optimal coating sample ($G_{3\%}TG_{2\%}$) displayed the highest generation rate of 8.4 µmol g^{-1} h^{-1} among the single- and double-sided modified samples, which was almost 3 times as that of $G_{3\%}T$ sample (Fig. 11e). As the scheme shown in Fig. 11f [133], the graphene sheets can effectively collect and separate photogenerated electrons, but only work on those that can conduct to their surface in a short distance. The double-sided modification method greatly increases the contact area of the shell with graphene sheets, which is beneficial for graphene to separate more photoelectrons from both the inner and outer sides of the shell simultaneously.

In addition to CH_4 gas, the CO_2 photoreduction may produce other chemicals, such as carbon monoxide (CO), hydrogen (H_2), oxygen (O_2), methanol (CH_3OH), and others. Table 5 lists a few photoreduction products as catalyzed by some typical CSSG catalysts [133–139]. The product selectivity and evolution rate chiefly rely on the adsorption/desorption properties of reactants/intermediates as well as the photocatalytic activity of catalysts [140].

6 Summary and Perspectives

In conclusion, this review highlights the CSSG nanoarchitectures for photocatalytic performance. The categories of CSSG nanomaterials along with the synthesis method, physicochemical properties, and photocatalytic performances are systematically discussed and analyzed. The CSSG nanomaterials exist in the morphologies of 0D, 1D, 2D, and 3D, which can be constructed by the internal and external driving forces. The binding effect, the amount and lattice characteristics of the graphene sheets, the photoelectric modulation of the semiconductor component, the defect states, and charge transport of the hybrid materials can be assessed by characterizing the morphology and structure, optical, and electrochemical properties of the specimens. The CSSG nanoarchitectures address key challenges of the individual semiconductors and offer opportunities for the development of more efficient and reliable photocatalysis, crucial for the future of environmental remedy and sustainable energy.

Although great achievements have been made in CSSG nanoarchitectures, several issues should be addressed in future research: (1) Uniform shell growth. To ensure the uniformity and precise control of the shell thickness and crystal structure, novel growth methods can be used for exploration. This may involve refining existing techniques, combining different construction methods, or developing new approaches to achieve consistent shell thickness across a range of core materials. (2) Core–shell modulation. It should focus on tailoring the graphene sheets, including the graphene type and layer number based on the specific physical and chemical properties of the semiconductor component. Meanwhile, the semiconductor should be regulated with an ideal composition and content. This
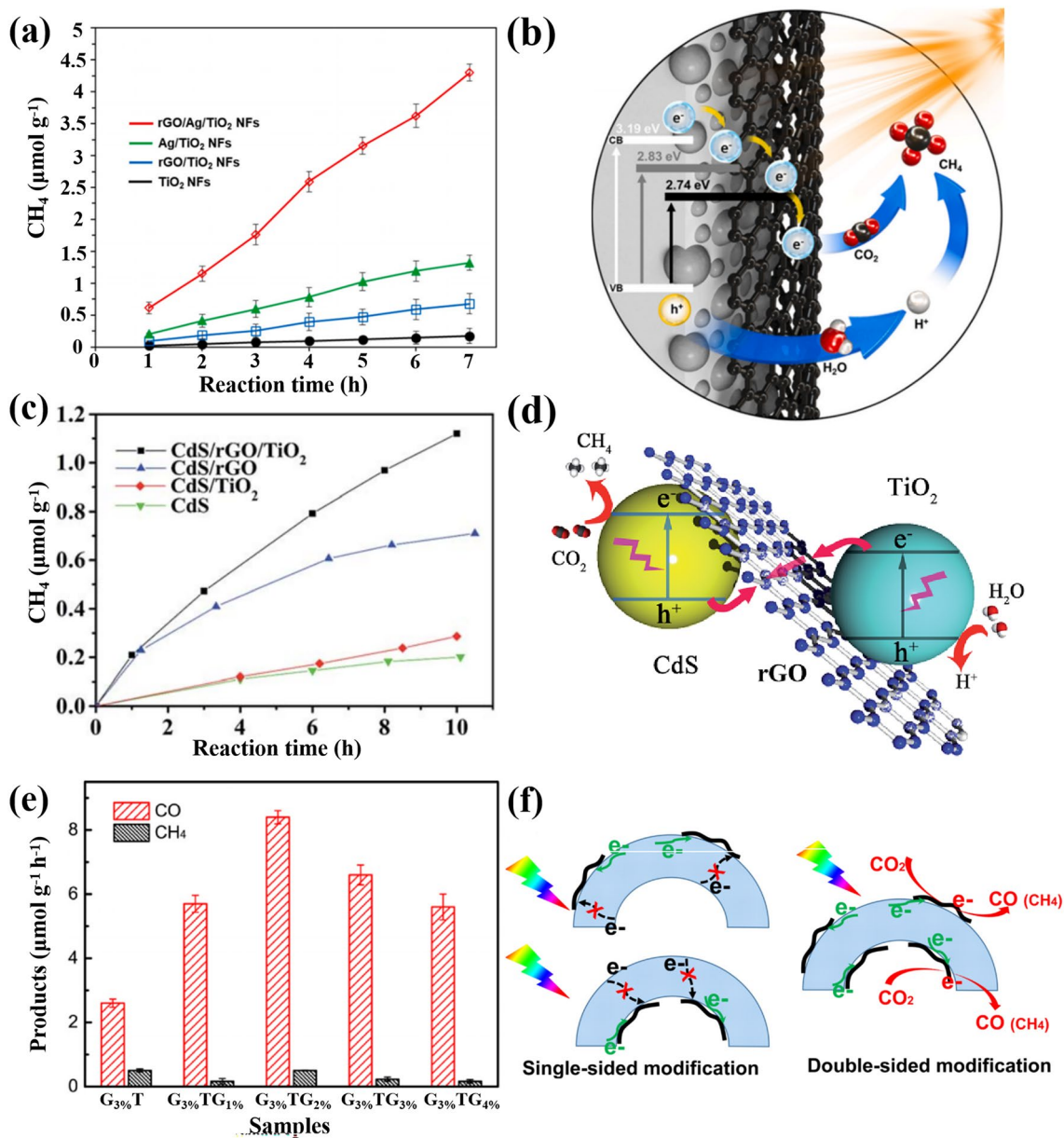
Fig. 11 Methane (CH_4) and carbon monoxide (CO) evolutions as catalyzed by different CSSG materials and their enhancement mechanisms: **a, b** TiO_2/Ag/rGO (reproduced with permission from Ref. [52]. Copyright 2022 Elsevier Publishing). **c, d** CdS/rGO/TiO_2 (reproduced with permission from Ref. [73]. Copyright 2015 RSC Publishing). **e, f** G/TiO_2/G (reproduced with permission from Ref. [133]. Copyright 2020 Elsevier Publishing)

customization can lead to CSSG nanomaterials with optimal photoelectrochemical properties for various applications. On the other hand, the graphene can be replaced by other carbon group compounds to further improve the performance of photocatalysis, such as a novel allotrope graphdiyne. Compared with graphene, graphdiyne is rich in carbon chemical bonds and tall conjugated systems,

leading to strong chemical reactivity with special semiconductor characteristics [141]. The core–shell structure and synergistic interaction between graphdiyne and other semiconductors can greatly improve the electric conductivity, facilitate the mass/ion transport and gas emissions, and expose more active sites [142]. The combination can also create a S-scheme heterojunction for the effective

Table 5 Comparison of photocatalytic activity of some typical CSSG nanomaterials for CO_2 reduction

Material	Light source	Fuel	Formation rate	Apparent quantum efficiency (%)	References
CdS NSs	Xenon 300 W, distance 10 cm	CH_4	21 μmol g^{-1} h^{-1}	–	[73]
CdS/TiO$_2$ NSs	Xenon 300 W, distance 10 cm	CH_4	29.4 μmol g^{-1} h^{-1}	–	
CdS/rGO NSs	Xenon 300 W, distance 10 cm	CH_4	63 μmol g^{-1} h^{-1}	–	
CdS/rGO/TiO$_2$ NSs	Xenon 300 W, distance 10 cm	CH_4	~117.6 μmol g^{-1} h^{-1}	–	
TiO$_2$ NFs	Xenon 500 W, 10 mW cm^{-2}	CH_4	~0.20 μmol g^{-1} in 7 h	–	[52]
TiO$_2$/rGO NFs	Xenon 500 W, 10 mW cm^{-2}	CH_4	~0.70 μmol g^{-1} in 7 h	–	
TiO$_2$/Ag NFs	Xenon 500 W, 10 mW cm^{-2}	CH_4	~1.30 μmol g^{-1} in 7 h	–	
TiO$_2$/Ag/rGO NFs	Xenon 500 W, 10 mW cm^{-2}	CH_4	4.30 μmol g^{-1} in 7 h	–	
TiO$_2$/rGO NPs	Xenon 300 W, 80 mW cm^{-2}	CH_4	6.0 μmol g^{-1} h^{-1}	0.30	[134]
TiO$_2$/Pt NPs	Xenon 300 W, 80 mW cm^{-2}	CH_4	13.3 μmol g^{-1} h^{-1}	0.65	
TiO$_2$/Pt/rGO NPs	Xenon 300 W, 80 mW cm^{-2}	CH_4	41.3 μmol g^{-1} h^{-1}	1.93	
rTiO$_2$/Cu-Pt/G NPs	Sunlight simulator 1000 W m^{-2}	CO	394.84 μmol g^{-1} h^{-1}	23.77	[135]
TiO$_2$/rGO hollow MSs	Xenon 300 W	CO	3.4 μmol g^{-1} h^{-1}	–	[133]
rGO/TiO$_2$ hollow MSs	Xenon 300 W	CO	2.6 μmol g^{-1} h^{-1}	–	
rGO/TiO$_2$/rGO MSs	Xenon 300 W	CO	8.4 μmol g^{-1} h^{-1}	0.034	
TaON NPs	Xenon 300 W	CH_4	0.12 μmol g^{-1} h^{-1}	0.03	[136]
TaON/G NPs	Xenon 300 W	CH_4	1.61 μmol g^{-1} h^{-1}	0.41	
CsPbBr$_3$ NPs	Xenon 500 W, 100 mW cm^{-2}	CH_4/ H_2	13.9/ 4.7 μmol g^{-1} h^{-1}	–	[137]
CsPbBr$_3$/GO NPs	Xenon 500 W, 100 mW cm^{-2}	CH_4/ H_2	18.6/ 6.9 μmol g^{-1} h^{-1}	–	
CsPbBr$_3$/G NPs	Xenon 500 W, 100 mW cm^{-2}	CH_4/ H_2	4.7/ 3.9 μmol g^{-1} h^{-1}	–	
Fe$_3$O$_4$ MSs	White LED 20 W, 85 W/m^2	CH_3OH	278 μmol g^{-1} in 24 h	0.26	[138]
Fe$_3$O$_4$/CuZnO MSs	White LED 20 W, 85 W m^{-2}	CH_3OH	858 μmol g^{-1} in 24 h	0.82	
Fe$_3$O$_4$/CuZnO/GO MSs	White LED 20 W, 85 W m^{-2}	CH_3OH	1749 μmol g^{-1} in 24 h	1.67	
Fe$_3$O$_4$/CuZnO/rGO MSs	White LED 20 W, 85 W m^{-2}	CH_3OH	2656 μmol g^{-1} in 24 h	2.53	
ZnO NPs	Xenon 300 W, distance 10 cm	CO/O$_2$/CH$_3$OH	1.26/ 0.85/ 0.31 μmol g^{-1} h^{-1}	–	[139]
ZnO/G NPs	Xenon 300 W, distance 10 cm	CO/O$_2$/CH$_3$OH	3.38/ 1.35/ 0.59 μmol g^{-1} h^{-1}	–	

charge separation [143] and thus enhance the catalytic activity and long-term stability. (3) Functional maximization. Except for the graphene and semiconductor, other components can also be introduced in the CSSG structures to enhance the functionality [144, 145]. For example, noble metal NPs can be encapsulated to improve the photocatalytic performance for the localized surface plasmon characteristics. The single semiconductor component can be replaced by the heterogeneous semiconductors as the latter can extend light absorption and reduce charge recombination. (4) Application extension. Besides aforementioned applications, the CSSG nanoarchitectures can also be active catalysts in other photocatalytic reactions, just like semiconductor photocatalysts in the generation of hydrogen peroxide (H_2O_2), organic fuels and special radicals, removal of air pollutants and hazard substances,

fabrication of batteries and capacitors, inactivation of bacteria, and so on [146–151]. It is conceivable that the CSSG nanoarchitectures will perform better than single semiconductor or other kinds of semiconductor/graphene composite photocatalysts for their superior core–shell structure and physicochemical properties. Moreover, the function of the CSSG nanoarchitectures is not only limited to photocatalysis, but also has important applications in electrocatalysis, photoelectronics, supercapacitors, lithium-ion batteries, and others. (5) Mechanism illustration. Although photocatalytic mechanisms and synergistic effects of the CSSG catalysts are clear at present, the detailed functional electrocatalytic sites, wavelength-dependent charge transfer in the heterostructures, precise quantity of photogenerated electrons, reaction kinetics, doping and vacancy contributions, etc., are still elusive in most cases. Novel

technologies may be used for the illustration, such as in situ irradiated X-ray photoelectron spectroscopy [152, 153] and total internal reflectance fluorescence microscopy [132]. (6) Streamlined processes. Simplifying and optimizing the synthesis processes for CSSG nanoarchitectures can lead to more efficient and cost-effective production methods, which can facilitate the scalability and industrialization of these materials. (7) Industrialization. The transition from laboratory-scale production to large-scale industrialization requires careful consideration of the scalability, cost-effectiveness, and reproducibility. Research efforts should aim to bridge the gap between small-scale research and commercial production.

Author Contributions Jinshen Lan contributed to investigation, data curation, original draft writing, and conceptualization. Shanzhi Qu was involved in data curation, figure design, and conceptualization. Xiaofang Ye contributed to data curation, figure design, and conceptualization. Yifan Zheng was involved in conceptualization. Mengwei Ma contributed to conceptualization. Shengshi Guo was involved in conceptualization. Shengli Huang contributed to figure design, conceptualization, validation, original draft writing, review and editing, and supervision. Shuping Li was involved in conceptualization and review and editing. Junyong Kang contributed to conceptualization and review and editing.

Declarations

References

1. F. Wang, Q. Li, D. Xu, Recent progress in semiconductor-based nanocomposite photocatalysts for solar-to-chemical energy conversion. Adv. Energy Mater. **7**, 1700529 (2017). https://doi.org/10.1002/aenm.201700529

2. H. Zhou, Y. Qu, T. Zeida, X. Duan, Towards highly efficient photocatalysts using semiconductor nanoarchitectures. Energy Environ. Sci. **5**, 6732 (2012). https://doi.org/10.1039/c2ee03447f

3. Z.H. Jabbar, S.E. Ebrahim, Recent advances in nano-semiconductors photocatalysis for degrading organic contaminants and microbial disinfection in wastewater: a comprehensive review. Environ. Nanotechnol. Monit. Manage. **17**, 100666 (2022). https://doi.org/10.1016/j.enmm.2022.100666

4. L. Zhang, M. Jaroniec, Toward designing semiconductor-semiconductor heterojunctions for photocatalytic applications. Appl. Surf. Sci. **430**, 2–17 (2018). https://doi.org/10.1016/j.apsusc.2017.07.192

5. M. Pirhashemi, A. Habibi-Yangjeh, S.R. Pouran, Review on the criteria anticipated for the fabrication of highly efficient ZnO-based visible-light-driven photocatalysts. J. Ind. Eng. Chem. **62**, 1–25 (2018). https://doi.org/10.1016/j.jiec.2018.01.012

6. H. Wang, L. Zhang, Z. Chen, J. Hu, S. Li et al., Semiconductor heterojunction photocatalysts: design, construction, and photocatalytic performances. Chem. Soc. Rev. **43**, 5234 (2014). https://doi.org/10.1039/c4cs00126e

7. C. Feng, Z.-P. Wu, K.-W. Huang, J. Ye, H. Zhang, Surface modification of 2D photocatalysts for solar energy conversion. Adv. Mater. **34**, 2200180 (2022). https://doi.org/10.1002/adma.202200180

8. S.A. Jitan, G. Palmisano, C. Garlisi, Synthesis and surface modification of TiO_2-based photocatalysts for the conversion of CO_2. Catalysts **10**, 227 (2020). https://doi.org/10.3390/catal10020227

9. L. Jiang, X. Huang, Y. Zhou, S. Huang, Y. Wang et al., High photocatalytic performance of ferroelectric $AgNbO_3$ in a doping state. J. Environ. Chem. Eng. **11**, 110402 (2023). https://doi.org/10.1016/j.jece.2023.110402

10. T. Xu, X. Liu, S. Wang, L. Li, Ferroelectric oxide nanocomposites with trimodal pore structure for high photocatalytic performance. Nano-Micro Lett. **11**, 37 (2019). https://doi.org/10.1007/s40820-019-0268-y

11. Y. Li, L. Wang, F. Zhang, W. Zhang, G. Shao et al., Detecting and quantifying wavelength-dependent electrons transfer in heterostructure catalyst via in situ irradiation XPS. Adv. Sci. **10**, 2205020 (2023). https://doi.org/10.1002/advs.202205020

12. L. Wang, Y. Li, Y. Ai, E. Fan, F. Zhang et al., Tracking heterogeneous interface charge reverse separation in $SrTiO_3$/NiO/NiS nanofibers with in situ irradiation XPS. Adv. Funct. Mater. **33**, 2306466 (2023). https://doi.org/10.1002/adfm.202306466

13. S. Liu, N. Zhang, Y.-J. Xu, Core–shell structured nanocomposites for photocatalytic selective organic transformations.

Part. Part. Syst. Charact. **31**, 540–556 (2014). https://doi.org/10.1002/ppsc.201300235

14. A. Shafiee, N. Rabiee, S. Ahmadi, M. Baneshi, M. Khatami et al., Core−shell nanophotocatalysts: Review of materials and applications. ACS Appl. Nano Mater. **5**, 55–86 (2022). https://doi.org/10.1021/acsanm.1c03714

15. S. Wang, Y. Zhang, Y. Zheng, Y. Xu, G. Yang et al., Plasmonic metal mediated charge transfer in stacked core–shell semiconductor heterojunction for significantly enhanced CO_2 photoreduction. Small **19**, 2204774 (2023). https://doi.org/10.1002/smll.202204774

16. D. He, C. Zhang, G. Zeng, Y. Yang, D. Huang et al., A multifunctional platform by controlling of carbon nitride in the core-shell structure: from design to construction, and catalysis applications. Appl. Catal. B-Environ. **258**, 117957 (2019). https://doi.org/10.1016/j.apcatb.2019.117957

17. I. Khan, N. Baig, S. Ali, M. Usman, S.A. Khan et al., Progress in layered cathode and anode nanoarchitectures for charge storage devices: challenges and future perspective. Energy Storage Mater. **35**, 443–469 (2021). https://doi.org/10.1016/j.ensm.2020.11.033

18. W. Luo, S. Zafeiratos, A brief review of the synthesis and catalytic applications of graphene-coated oxides. ChemCatChem **9**, 2432–2442 (2017). https://doi.org/10.1002/cctc.201700178

19. W. Lu, L. Guo, Y. Jia, Y. Guo, Z. Li et al., Significant enhancement in photocatalytic activity of high quality SiC/graphene core–shell heterojunction with optimal structural parameters. RSC Adv. **4**, 46771 (2014). https://doi.org/10.1039/c4ra06026a

20. N. Gao, X. Fang, Synthesis and development of graphene−inorganic semiconductor nanocomposites. Chem. Rev. **115**, 8294–8343 (2015). https://doi.org/10.1021/cr400607y

21. J.S. Lee, K.H. You, C.B. Park, Highly photoactive, low bandgap TiO_2 nanoparticles wrapped by graphene. Adv. Mater. **24**, 1084–1088 (2012). https://doi.org/10.1002/adma.201104110

22. S. Lin, Y. Lu, J. Xu, S. Feng, J. Li, High performance graphene/semiconductor van der Waals heterostructure optoelectronic devices. Nano Energy **40**, 122–148 (2017). https://doi.org/10.1016/j.nanoen.2017.07.036

23. H.T. Tung, H.K. Dan, D. Thomas, H.K. Jun, L.T.N. Tu, The preparation of reduced graphene oxide—Cu_2S by hydrothermal method for quantum dot sensitized solar cells. Opt. Mater. **139**, 113725 (2023). https://doi.org/10.1016/j.optmat.2023.113725

24. H. Yin, G. Zhan, R. Yan, X. Wu, Q. Hu et al., P–n heterogeneous Sb_2S_3/SnO_2 quantum dot anchored reduced graphene oxide nanosheets for high-performance lithium-ion batteries. Dalton Trans. **53**, 7142–7151 (2024). https://doi.org/10.1039/d4dt00153b

25. L. Syam-Sundar, M. Amin-Mir, M. Waqar-Ashraf, F. Djavanroodi, Synthesis and characterization of graphene and its composites for Lithium-Ion battery applications: a comprehensive review. Alex. Eng. J. **78**, 224–245 (2023). https://doi.org/10.1016/j.aej.2023.07.044

26. R. Hou, S. Zhang, Y. Zhang, N. Li, S. Wang et al., A "three-region" configuration for enhanced electrochemical kinetics and high-areal capacity lithium–sulfur batteries. Adv. Funct. Mater. **32**, 2200302 (2022). https://doi.org/10.1002/adfm.202200302

27. Y. Zhang, Z. Wu, S. Wang, N. Li, S.R.P. Silva et al., Complex permittivity-dependent plasma confinementassisted growth of asymmetric vertical graphene nanofiber membrane for high-performance Li-S full cells. InfoMat **4**, e12294 (2022). https://doi.org/10.1002/inf2.12294

28. S. Nongthombam, N.A. Devi, S. Sinha, R. Bhujel, S. Rai et al., Reduced graphene oxide/gallium nitride nanocomposites for supercapacitor applications. J. Phys. Chem. Solids **141**, 109406 (2020). https://doi.org/10.1016/j.jpcs.2020.109406

29. S. Nagarani, G. Sasikala, M. Yuvaraj, R. Dhilip-Kumar, S. Balachandran et al., ZnO-CuO nanoparticles enameled on reduced graphene nanosheets as electrode materials for supercapacitors applications. J. Energy Storage **52**, 104969 (2022). https://doi.org/10.1016/j.est.2022.104969

30. H. Tian, A. Hu, Q. Liu, X. He, X. Guo, Interface-induced high responsivity in hybrid graphene/GaAs photodetector. Adv. Optical Mater. **2020**, 1901741 (2020). https://doi.org/10.1002/adom.201901741

31. M.A. Iqbal, N. Anwar, M. Malik, M. Al-Bahrani, M.R. Islam et al., Nanostructures/graphene/silicon junction-based high-performance photodetection systems: progress, challenges, and future trends. Adv. Mater. Interfaces **10**, 2202208 (2023). https://doi.org/10.1002/admi.202202208

32. Y. Hu, C. Zhou, H. Wang, M. Chen, G. Zeng et al., Recent advance of graphene/semiconductor composite nanocatalysts: synthesis, mechanism, applications and perspectives. Chem. Eng. J. **414**, 128795 (2021). https://doi.org/10.1016/j.cej.2021.128795

33. M.A. Ahmed, A.A. Mohamed, Recent progress in semiconductor/graphene photocatalysts: synthesis, photocatalytic applications, and challenges. RSC Adv. **13**, 421 (2023). https://doi.org/10.1039/d2ra07225d

34. A. Mondal, A. Prabhakaran, S. Gupta, V.R. Subramanian, Boosting photocatalytic activity using reduced graphene oxide (RGO)/semiconductor nanocomposites: issues and future scope. ACS Omega **6**, 8734–8743 (2021). https://doi.org/10.1021/acsomega.0c06045

35. Y. Chen, B.Y. Zhai, Y.N. Liang, Y. Li, Hybrid photocatalysts using semiconductor/MOF/graphene oxide for superior photodegradation of organic pollutants under visible light. Mat. Sci. Semicon. Proc. **107**, 104838 (2020). https://doi.org/10.1016/j.mssp.2019.104838

36. C. He, X. Bu, S. Yang, P. He, G. Ding et al., Core-shell $SrTiO_3$/graphene structure by chemical vapor deposition for enhanced photocatalytic performance. Appl. Surf. Sci. **436**, 373–381 (2018). https://doi.org/10.1016/j.apsusc.2017.12.063

37. Y. Zhang, D. Li, Y. Zhang, X. Zhou, S. Guo et al., Graphene-wrapped $Bi_2O_2CO_3$ core–shell structures with enhanced quantum efficiency profit from an ultrafast electron transfer

process. J. Mater. Chem. A **2**, 8273 (2014). https://doi.org/10.1039/c4ta00088a

38. D. Shao, M. Yu, H. Sun, T. Hu, J. Lian et al., High responsivity, fast ultraviolet photodetector fabricated from ZnO nanoparticle–graphene core–shell structures. Nanoscale **5**, 3664 (2013). https://doi.org/10.1039/c3nr00369h

39. L. Yu, Q. Yang, G. Zhu, R. Che, Preparation and lithium storage of core–shell honeycomb-like Co_3O_4@C microspheres. RSC Adv. **12**, 29818 (2022). https://doi.org/10.1039/d2ra05204k

40. W. Zhou, J. Zhu, C. Cheng, J. Liu, H. Yang et al., A general strategy toward graphene@metal oxide core–shell nanostructures for high-performance lithium storage. Energy Environ. Sci. **4**, 4954 (2011). https://doi.org/10.1039/c1ee02168k

41. Q. Wu, L. Yang, X. Wang, Z. Hu, Carbon-based nanocages: a new platform for advanced energy storage and conversion. Adv. Mater. **32**, 1904177 (2020). https://doi.org/10.1002/adma.201904177

42. M.I.A. Abdel-Maksoud, R.A. Fahim, A.E. Shalan, M. Abd-Elkodous, S.O. Olojede et al., Advanced materials and technologies for supercapacitors used in energy conversion and storage: a review. Environ. Chem. Lett. **19**, 375–437 (2021). https://doi.org/10.1007/s10311-020-01075-w

43. H. Zhang, D. Yang, A. Lau, T. Ma, H. Lin et al., Hybridized graphene for supercapacitors: beyond the limitation of pure graphene. Small **17**, 2007311 (2021). https://doi.org/10.1002/smll.202007311

44. H. Feng, L. Tang, G. Zeng, J. Tang, Y. Deng et al., Carbon-based core–shell nanostructured materials for electrochemical energy storage. J. Mater. Chem. A **6**, 7310 (2018). https://doi.org/10.1039/c8ta01257a

45. K.S. Lee, J. Shim, J.S. Lee, J. Lee, H.G. Moon et al., Adsorption behavior of NO_2 molecules in ZnO-mono/multilayer graphene core–shell quantum dots for NO_2 gas sensor. J. Ind. Eng. Chem. **106**, 279–286 (2022). https://doi.org/10.1016/j.jiec.2021.11.003

46. X. Chen, Y. Zhan, A. Sun, Q. Feng, W. Yang et al., Anchoring the TiO_2@crumpled graphene oxide core–shell sphere onto electrospun polymer fibrous membrane for the fast separation of multi-component pollutant-oil–water emulsion. Sep. Purif. Technol. **298**, 121605 (2022). https://doi.org/10.1016/j.seppur.2022.121605

47. M.M. Tavakoli, H. Aashuri, A. Simchi, S. Kalytchuk, Z. Fan, Quasi core/shell lead sulfide/graphene quantum dots for bulk heterojunction solar cells. J. Phys. Chem. C **119**, 18886–18895 (2015). https://doi.org/10.1021/acs.jpcc.5b04195

48. P. Shankar, M.Q. Hafzan-Ishak, J.K. Padarti, N. Mintcheva, S. Iwamori et al., ZnO@graphene oxide core@shell nanoparticles prepared via one-pot approach based on laser ablation in water. Appl. Surf. Sci. **531**, 147365 (2020). https://doi.org/10.1016/j.apsusc.2020.147365

49. D.I. Son, B.W. Kwon, D.H. Park, W.-S. Seo, Y. Yi et al., Emissive ZnO–graphene quantum dots for white-light-emitting diodes. Nat. Nanotechnol. **7**, 465–471 (2012). https://doi.org/10.1038/nnano.2012.71

50. Y. Fei, X. Ye, A.S. Al-Baldawy, J. Wan, J. Lan et al., Enhanced photocatalytic performance of TiO_2 nanowires by substituting noble metal particles with reduced graphene oxide. Curr. Appl. Phys. **44**, 33–39 (2022). https://doi.org/10.1016/j.cap.2022.09.008

51. X. Li, Y. Zhang, T. Li, Q. Zhong, H. Li et al., Graphene nanoscrolls encapsulated TiO_2 (B) nanowires for lithium storage. J. Power. Sources **268**, 372–378 (2014). https://doi.org/10.1016/j.jpowsour.2014.06.056

52. S. Kang, J. Hwang, rGO-wrapped Ag-doped TiO_2 nanofibers for photocatalytic CO_2 reduction under visible light. J. Clean. Prod. **374**, 134022 (2022). https://doi.org/10.1016/j.jclepro.2022.134022

53. D. Kathiravan, B.-R. Huang, A. Saravanan, Self-assembled hierarchical interfaces of ZnO nanotubes/graphene heterostructures for efficient room temperature hydrogen sensors. ACS Appl. Mater. Interfaces **9**, 12064–12072 (2017). https://doi.org/10.1021/acsami.7b00338

54. X. Ye, Y. Tian, M. Gao, F. Cheng, J. Lan et al., Efficient photocatalytic core–shell synthesis of titanate nanowire/rGO. Catalysts **14**, 218 (2024). https://doi.org/10.3390/catal14040218

55. H.-J. Kim, S.E. Lee, J. Lee, J.-Y. Jung, E.-S. Lee et al., Gold-coated silicon nanowire–graphene core–shell composite film as a polymer binder-free anode for rechargeable lithium-ion batteries. Physica E **61**, 204–209 (2014). https://doi.org/10.1016/j.physe.2014.03.030

56. S.M. Ji, A.P. Tiwari, H.Y. Kim, Graphene oxide coated zinc oxide core–shell nanofibers for enhanced photocatalytic performance and durability. Coatings **10**, 1183 (2020). https://doi.org/10.3390/coatings10121183

57. Y. Jia, X. Jiang, A. Ahmed, L. Zhou, Q. Fan et al., Microfluidic spinning of core–shell α-MnO_2@graphene fibers with porous network structure for all-solid-state flexible supercapacitors. J. Electrochem. Soc. **168**, 070514 (2021). https://doi.org/10.1149/1945-7111/ac0f85

58. H. Yu, P. Joo, D. Lee, B.-S. Kim, J.H. Oh, Photoinduced charge-carrier dynamics of phototransistors based on perylene diimide/reduced graphene oxide core/shell p–n junction nanowires. Adv. Optical Mater. **3**, 241–247 (2015). https://doi.org/10.1002/adom.201400346

59. D. Xia, Q. Xue, J. Xie, H. Chen, C. Lv, Silicon/graphene core/shell nanowires produced by self-scrolling. Comp. Mater. Sci. **49**, 588–592 (2010). https://doi.org/10.1016/j.commatsci.2010.05.053

60. J. Lin, H. Jia, H. Liang, S. Chen, Y. Cai et al., In situ synthesis of vertical standing nanosized NiO encapsulated in graphene as electrodes for highperformance supercapacitors. Adv. Sci. **5**, 1700687 (2018). https://doi.org/10.1002/advs.201700687

61. J. Yus, Y. Bravo, A.J. Sanchez-Herencia, B. Ferrari, Z. Gonzalez, Electrophoretic deposition of RGO-NiO core-shell nanostructures driven by heterocoagulation method with high electrochemical performance. Electrochim. Acta **308**, 363–372 (2019). https://doi.org/10.1016/j.electacta.2019.04.053

62. F. Kirschvink, M. Stürzel, Y. Thomann, R. Mülhaupt, Gas phase mineralized graphene as core/shell nanosheet supports for single-site olefin polymerization catalysts and in-situ formation of graphene/polyolefin nanocomposites. Polymer **55**, 4547–4550 (2014). https://doi.org/10.1016/j.polymer.2014.07.017

63. Q. Liu, S. Wang, Q. Ren, T. Li, G. Tu et al., Stacking design in photocatalysis: synergizing cocatalyst roles and anti-corrosion functions of metallic MoS_2 and graphene for remarkable hydrogen evolution over CdS. J. Mater. Chem. A **9**, 1552 (2021). https://doi.org/10.1039/d0ta10255e

64. L. Han, Y.N. Hao, X. Wei, X.W. Chen, Y. Shu et al., Hollow copper sulfide nanosphere−doxorubicin/graphene oxide core−shell nanocomposite for photothermo-chemotherapy. ACS Biomater. Sci. Eng. **3**, 3230–3235 (2017). https://doi.org/10.1021/acsbiomaterials.7b00643

65. S. Bera, A. Naskar, M. Pal, S. Jana, Low temperature synthesis of graphene hybridized surface defective hierarchical core–shell structured ZnO hollow microspheres with longterm stable and enhanced photoelectrochemical activity. RSC Adv. **6**, 36058 (2016). https://doi.org/10.1039/c6ra03410a

66. E. Vasilaki, N. Katsarakis, S. Dokianakis, M. Vamvakaki, rGO functionalized ZnO–TiO$_2$ core-shell flower-like architectures for visible light photocatalysis. Catalysts **11**, 332 (2021). https://doi.org/10.3390/catal11030332

67. H. Liu, T. Lv, Z. Zhu, Template-assisted synthesis of hollow TiO_2@rGO core–shell structural nanospheres with enhanced photocatalytic activity. J. Mol. Catal. A-Chem. **404–405**, 178–185 (2015). https://doi.org/10.1016/j.molcata.2015.04.022

68. D. Zhang, Q. Wei, H. Huang, L. Jiang, J. Teng et al., Ambient-condition strategy for production of hollow Ga_2O_3@rGO crystalline nanostructures toward efficient lithium storage. Energy Environ. Mater. **7**, e12585 (2024). https://doi.org/10.1002/eem2.12585

69. Y. Zhao, X. Zhang, C. Wang, Y. Zhao, H. Zhou et al., The synthesis of hierarchical nanostructured MoS_2/graphene composites with enhanced visible-light photo-degradation property. Appl. Surf. Sci. **412**, 207–213 (2017). https://doi.org/10.1016/j.apsusc.2017.03.181

70. W. Zhai, Q. Ai, L. Chen, S. Wei, D. Li et al., Walnut-inspired microsized porous silicon/graphene core–shell composites for high-performance lithium-ion battery anodes. Nano Res. **10**, 4274–4283 (2017). https://doi.org/10.1007/s12274-017-1584-5

71. Y. Bu, Z. Chen, W. Li, Dramatically enhanced photocatalytic properties of Ag-modified graphene–ZnO quasi-shell–core heterojunction composite material. RSC Adv. **3**, 24118 (2013). https://doi.org/10.1039/c3ra44047h

72. Y. Zhang, L. Song, Y. Zhang, P. Wang, Y. Liu et al., A facile method for synthesis of well-coated ZnO@graphene core/shell structure by self-assembly of amine-functionalized ZnO and graphene oxide. Chem. Phys. Lett. **654**, 107–113 (2016). https://doi.org/10.1016/j.cplett.2016.05.023

73. L. Kuai, Y. Zhou, W. Tu, P. Li, H. Li et al., Rational construction of a CdS/reduced graphene oxide/TiO$_2$ core–shell nanostructure as an allsolid-state Z-scheme system for CO_2 photoreduction into solar fuels. RSC Adv. **5**, 88409 (2015). https://doi.org/10.1039/c5ra14374h

74. I. John-Peter, N. Rajamanickam, S. Vijaya, S. Anandan, K. Ramachandran et al., TiO$_2$/graphene quantum dots core-shell based photo anodes with TTIP treatment—a perspective way of enhancing the short circuit current. Sol. Energy Mat. Sol. C. **205**, 110239 (2020). https://doi.org/10.1016/j.solmat.2019.110239

75. C. Zou, D. Ma, Y. Su, M. Zhu, B. Zhou et al., Three-dimensional Au nanoparticles-decorated γ-Fe$_2$O$_3$@reduced graphene oxide core-shell heterojunctions for highly sensitive room-temperature gas sensors. Ceram. Int. **48**, 37064–37074 (2022). https://doi.org/10.1016/j.ceramint.2022.08.281

76. Q. Wu, H. Bai, R. Zhao, A. Gao, H. Deng et al., Core-shell ZrO_2@GO hybrid for effective interfacial adhesion improvement of carbon fiber/epoxy composites. Surf. Interfaces **40**, 103070 (2023). https://doi.org/10.1016/j.surfin.2023.103070

77. M. Romero, V. Mello, C. Boher, A.P. Tschiptschin, C. Scandian, On the tribological behavior of cobalt-based nanocomposite coatings containing ZnO@Graphene oxide core-shell nanoparticles. Wear **522**, 204835 (2023). https://doi.org/10.1016/j.wear.2023.204835

78. C. Kim, C. Park, Formation of Al_2O_3-graphite core shells versus growth time by using thermal chemical vapor deposition. J. Korean Phys. Soc. **69**, 842–846 (2016). https://doi.org/10.3938/jkps.69.842

79. A.R. Biris, D. Toloman, A. Popa, M.D. Lazar, G.K. Kannarpady et al., Synthesis of tunable core–shell nanostructures based on TiO$_2$-graphene architectures and their application in the photodegradation of rhodamine dyes. Phys. E **81**, 326–333 (2016). https://doi.org/10.1016/j.physe.2016.03.028

80. M. Zubair, E.M.M. Vanhaecke, I.-H. Svenum, M. Rønning, J. Yang, Core-shell particles of C-doped CdS and graphene: a noble metal-free approach for efficient photocatalytic H_2 generation. Green Energy Environ. **5**, 461–472 (2020). https://doi.org/10.1016/j.gee.2020.10.017

81. Q. Wu, H. Bai, R. Zhao, Z. Ye, H. Deng et al., Amine-caged ZrO_2@GO multilayer core-shell hybrids in epoxy matrix for enhancing interfacial adhesion of carbon fiber composites. Compos. Part B-Eng. **245**, 110207 (2022). https://doi.org/10.1016/j.compositesb.2022.110207

82. S. Naghdi, A. Cherevan, A. Giesriegl, R. Guillet-Nicolas, S. Biswas et al., Selective ligand removal to improve accessibility of active sites in hierarchical MOFs for heterogeneous photocatalysis. Nat. Commun. **13**, 282 (2022). https://doi.org/10.1038/s41467-021-27775-7

83. J.K. Bristow, K.L. Svane, D. Tiana, J.M. Skelton, J.D. Gale et al., Free energy of ligand removal in the metal−organic framework UiO-66. J. Phys. Chem. C **120**, 9276–9281 (2016). https://doi.org/10.1021/acs.jpcc.6b01659

84. C. Frank-Rotsch, N. Dropka, F.-M. Kießling, P. Rudolph, Semiconductor crystal growth under the influence of

magnetic fields. Cryst. Res. Technol. **55**, 1900115 (2020). https://doi.org/10.1002/crat.201900115

85. A. Bagri, C. Mattevi, M. Acik, Y.J. Chabal, M. Chhowalla et al., Structural evolution during the reduction of chemically derived graphene oxide. Nat. Chem. **2**, 581–587 (2010). https://doi.org/10.1038/nchem.686

86. Z. Xiang, J. Qian, Y. Zhou, F. Liu, C. Qi et al., Synthesis of quasi-core–shell Co-doped ZnO/graphene nanoparticles. Mater. Lett. **161**, 286–288 (2015). https://doi.org/10.1016/j.matlet.2015.08.128

87. J. Zhang, L. Chen, Y. Wang, S. Cai, H. Yang et al., VO_2(B)/ Graphene composite-based symmetrical supercapacitor electrode via screen printing for intelligent packaging. Nanomaterials **8**, 1020 (2018). https://doi.org/10.3390/nano8121020

88. S. Mpelane, N. Mketo, M. Mlambo, N. Bingwa, P.N. Nomngongo, One-step synthesis of a Mn-doped Fe_2O_3/GO core–shell nanocomposite and its application for the adsorption of levofloxacin in aqueous solution. ACS Omega **7**, 23302–23314 (2022). https://doi.org/10.1021/acsomega.2c01460

89. R. Preetha, M. Govinda-raj, E. Vijayakumar, M.G. Narendran, B. Neppolian et al., Quasi-in situ synthesis of oxygen vacancy-enriched strontium iron oxide supported on boron-doped reduced graphene oxide to elevate the photocatalytic destruction of tetracycline. Langmuir **39**, 7091–7108 (2023). https://doi.org/10.1021/acs.langmuir.3c00340

90. Y.T. Xu, Y. Guo, L.X. Song, K. Zhang, M.M.F. Yuen et al., Co-reduction self-assembly of reduced graphene oxide nanosheets coated Cu_2O sub-microspheres core-shell composites as lithium ion battery anode materials. Electrochim. Acta **176**, 434–441 (2015). https://doi.org/10.1016/j.electacta.2015.06.093

91. D. Chen, H. Quan, J. Liang, L. Guo, One-pot synthesis of hematite@graphene core@shell nanostructures for superior lithium storage. Nanoscale **5**, 9684 (2013). https://doi.org/10.1039/c3nr03484d

92. R. Peng, Y. Li, J. Chen, P. Si, J. Feng et al., Reduced graphene oxide wrapped Au@ZnO core-shell structure for highly selective triethylamine gas sensing application at a low temperature. Sensor. Actuat. A-Phys. **283**, 128–133 (2018). https://doi.org/10.1016/j.sna.2018.09.063

93. Y. Khan, A.R. Urade, A.D. Adhikari, P.C. Maity, K. Ramesh et al., Electrochemical performance of binder-free Ni(OH)$_2$/ RGO battery type electrode materials for supercapacitor. Int. J. Green Energy **20**, 725–733 (2023). https://doi.org/10.1080/15435075.2022.2088238

94. A. Nekooei, M.R. Miroliaei, M.S. Nejad, H. Sheibani, Enhanced visible-light photocatalytic activity of ZnS/S-graphene quantum dots reinforced with Ag_2S nanoparticles. Mat. Sci. Eng. B-Adv. **284**, 115884 (2022). https://doi.org/10.1016/j.mseb.2022.115884

95. G. Hong, Q.-H. Wu, J. Ren, S.-T. Lee, Mechanism of nonmetal catalytic growth of graphene on silicon. Appl. Phys. Lett. **100**, 231604 (2012). https://doi.org/10.1063/1.4726114

96. W. Lu, D. Wang, L. Guo, Y. Jia, M. Ye et al., Bipolar carrier transfer channels in epitaxial graphene/SiC core–shell heterojunction for efficient photocatalytic hydrogen evolution. Adv.

Mater. **27**, 7986–7991 (2015). https://doi.org/10.1002/adma.201503606

97. A. Castellano-Soria, J. López-Sánchez, C. Granados-Miralles, M. Varela, E. Navarro et al., Novel one-pot sol-gel synthesis route of Fe_3C/few-layered graphene core/shell nanoparticles embedded in a carbon matrix. J. Alloy. Compd. **902**, 163662 (2022). https://doi.org/10.1016/j.jallcom.2022.163662

98. M. Kırkbınar, A. Demir, S. Altındal, F. Çalışkan, The effect of different rates of ultra-thin gossamer-like rGO coatings on photocatalytic performance in ZnO core-shell structures for optoelectronic applications. Diam. Relat. Mater. **130**, 109435 (2022). https://doi.org/10.1016/j.diamond.2022.109435

99. X. Tie, Q. Han, C. Liang, B. Li, J. Zai et al., Si@SiO$_x$/graphene nanosheets composite: Ball milling synthesis and enhanced lithium strorage performance. Front. Mater. **4**, 47 (2018). https://doi.org/10.3389/fmats.2017.00047

100. H. Tao, L. Xiong, S. Zhu, L. Zhang, X. Yang, Porous Si/C/ reduced graphene oxide microspheres by spray drying as anode for Li-ion batteries. J. Electroanal. Chem. **797**, 16–22 (2017). https://doi.org/10.1016/j.jelechem.2017.05.010

101. Q. Pan, P. Zuo, S. Lou, T. Mu, C. Du et al., Micro-sized spherical silicon@carbon@graphene prepared by spray drying as anode material for lithium-ion batteries. J. Alloy. Compd. **723**, 434–440 (2017). https://doi.org/10.1016/j.jallcom.2017.06.217

102. A. Jamaluddin, B. Umesh, F. Chen, J.-K. Chang, C.-Y. Su, Facile synthesis of core–shell structured Si@graphene balls as a high-performance anode for lithium-ion batteries. Nanoscale **12**, 9616 (2020). https://doi.org/10.1039/d0nr01346c

103. A. Jana, D.H. Gregory, Microwave-assisted synthesis of ZnO–rGO core–shell nanorod hybrids with photo- and electro-catalytic activity. Chem. Eur. J. **26**, 6703–6714 (2020). https://doi.org/10.1002/chem.202000535

104. C.L. Sun, C.T. Chang, H.H. Lee, J. Zhou, J. Wang et al., Microwave-assisted synthesis of a core-shell MWCNT/ GONR heterostructure for the electrochemical detection of ascorbic acid, dopamine, and uric acid. ACS Nano **5**, 7788–7795 (2011). https://doi.org/10.1021/nn2015908

105. R.K. Singh, R. Kumar, D.P. Singh, R. Savu, S.A. Moshkalev, Progress in microwave-assisted synthesis of quantum dots (graphene/carbon/semiconducting) for bioapplications: a review. Mater. Today Chem. **12**, 282–314 (2019). https://doi.org/10.1016/j.mtchem.2019.03.001

106. K. Xia, G. Wang, H. Zhang, Y. Yu, L. Liu et al., Synthesis and characterization of nitrogen-doped graphene hollow spheres as electrode material for supercapacitors. J. Nanopart. Res. **19**, 254 (2017). https://doi.org/10.1007/s11051-017-3954-z

107. M. Liu, M. Shi, W. Lu, D. Zhu, L. Li et al., Core–shell reduced graphene oxide/MnO$_x$@carbon hollow nanospheres for high performance supercapacitor electrodes. Chem. Eng. J. **313**, 518–526 (2017). https://doi.org/10.1016/j.cej.2016.12.091

108. C. Wang, J. Chen, Y. Shi, M. Zheng, Q. Dong, Preparation and performance of a core–shell carbon/sulfur material for

lithium/sulfur battery. Electrochim. Acta **55**, 7010–7015 (2010). https://doi.org/10.1016/j.electacta.2010.06.019

109. S.I. Ghazanlou, S.I. Ghazanlou, S.I. Ghazanlou, H. Karimi, N. Azimi et al., Multifunctional performance of core–shell rGO@Fe_3O_4 on the mechanical, electrical/thermal, EMI, and microstructure properties of cement-based composites. Constr. Build. Mater. **394**, 132182 (2023). https://doi.org/10.1016/j.conbuildmat.2023.132182

110. S.S.P. Haghshenas, A. Nemati, A. Simchi, C.-U. Kim, Dispute in photocatalytic and photoluminescence behavior in ZnO/graphene oxide core-shell nanoparticles. Mater. Lett. **240**, 117–120 (2019). https://doi.org/10.1016/j.matlet.2018.12.095

111. P. Makuła, M. Pacia, W. Macyk, How to correctly determine the band gap energy of modified semiconductor photocatalysts based on UV−Vis spectra. J. Phys. Chem. Lett. **9**, 6814–6817 (2018). https://doi.org/10.1021/acs.jpclett.8b02892

112. S. Qu, J. Wan, X. Ye, J. Lan, Y. Fei et al., Interfacial charge transfer of MoS_2/ZnO/Ag_2S nanotube array for efficient photocatalytic performance. J. Photoch. Photobio. A **447**, 115200 (2024). https://doi.org/10.1016/j.jphotochem.2023.115200

113. W.Y. Teoh, J.A. Scott, R. Amal, Progress in heterogeneous photocatalysis: from classical radical chemistry to engineering nanomaterials and solar reactors. J. Phys. Chem. Lett. **3**, 629–639 (2012). https://doi.org/10.1021/jz3000646

114. O. Defaoui, A. Boudjemaa, B. Sabrina, B. Hayoun, M. Bourouina et al., Kinetic modeling and experimental study of photocatalytic process using graphene oxide/TiO_2 composites. A case for wastewater treatment under sunlight. Reac. Kinet. Mech. Cat. **133**, 1141–1162 (2021)

115. Md. Rakibuddin, R. Ananthakrishnan, Effective photocatalytic dechlorination of 2,4-dichlorophenol by a novel graphene encapsulated ZnO/Co_3O_4 core–shell hybrid under visible light. Photochem. Photobiol. Sci. **15**, 86 (2016). https://doi.org/10.1039/c5pp00305a

116. H. Liu, X. Dong, X. Wang, C. Sun, J. Li et al., A green and direct synthesis of graphene oxide encapsulated TiO_2 core/shell structures with enhanced photoactivity. Chem. Eng. J. **230**, 279–285 (2013). https://doi.org/10.1016/j.cej.2013.06.092

117. X. Li, S. Zheng, C. Zhang, C. Hu, F. Chen et al., Synergistic promotion of photocatalytic performance by core@shell structured TiO_2/Au@rGO ternary photocatalyst. Mol. Catal. **438**, 55–65 (2017). https://doi.org/10.1016/j.mcat.2017.05.016

118. M. Wang, J. Han, H. Xiong, R. Guo, Yolk@shell nanoarchitecture of Au@r-GO/TiO_2 hybrids as powerful visible light photocatalysts. Langmuir **31**, 6220–6228 (2015). https://doi.org/10.1021/acs.langmuir.5b01099

119. H. Shen, X. Zhao, L. Duan, R. Liu, H. Wu et al., Influence of interface combination of RGO-photosensitized SnO_2@RGO core-shell structures on their photocatalytic performance. Appl. Surf. Sci. **391**, 627–634 (2017). https://doi.org/10.1016/j.apsusc.2016.06.031

120. D.V. Dao, T.T.N. Bich, N.T.T. Ha, W. Wang, T. Kim et al., Hematite Fe_2O_3@nitrogen-doped graphene core-shell photocatalyst for efficient cephalexin degradation under visible light irradiation. Ceram. Int. **48**, 34533–34542 (2022). https://doi.org/10.1016/j.ceramint.2022.08.037

121. Q. Gong, Y. Liua, Z. Dang, Core-shell structured Fe_3O_4@GO@MIL-100(Fe) magnetic nanoparticles as heterogeneous photo-Fenton catalyst for 2,4-dichlorophenol degradation under visible light. J. Hazard. Mater. **371**, 677–686 (2019). https://doi.org/10.1016/j.jhazmat.2019.03.019

122. C. Feng, Y. Deng, L. Tang, G. Zeng, J. Wang et al., Core-shell Ag_2CrO_4/N-GQDs@g-C_3N_4 composites with anti-photocorrosion performance for enhanced full-spectrum-light photocatalytic activities. Appl. Catal. B-Environ. **239**, 525–536 (2018). https://doi.org/10.1016/j.apcatb.2018.08.049

123. L. Allagui, B. Chouchene, T. Gries, G. Medjahdi, E. Girot et al., Core/shell rGO/BiOBr particles with visible photocatalytic activity towards water pollutants. Appl. Surf. Sci. **490**, 580–591 (2019). https://doi.org/10.1016/j.apsusc.2019.06.091

124. F. Gao, Q. Wan, J. Yuan, R. Lei, S. Lin et al., Highly efficient and durable core-shell catalyst with dual functions: Tungsten nitride quantum dots encapsulated in ultra-thin graphene. Appl. Catal. B-Environ. **299**, 120692 (2021). https://doi.org/10.1016/j.apcatb.2021.120692

125. N. Thangavel, S. Bellamkonda, A.D. Arulraj, G.R. Rao, B. Neppolian, Visible light induced efficient hydrogen production through semiconductor–conductor–semiconductor (S–C–S) interfaces formed between g-C_3N_4 and rGO/Fe_2O_3 core–shell composites. Catal. Sci. Technol. **8**, 5081 (2018). https://doi.org/10.1039/c8cy01248b

126. R.A. Rather, S. Singh, B. Pal, Core–shell morphology of Au-TiO_2@graphene oxide nanocomposite exhibiting enhanced hydrogen production from water. J. Ind. Eng. Chem. **37**, 288–294 (2016). https://doi.org/10.1016/j.jiec.2016.03.039

127. H. Jung, J. Song, S. Lee, Y.W. Lee, D.H. Wi et al., Hierarchical metal–semiconductor–graphene ternary heteronanostructures for plasmonenhanced wide-range visible-light photocatalysis. J. Mater. Chem. A **7**, 15831 (2019). https://doi.org/10.1039/c9ta03934a

128. M. Zubair, I.-H. Svenum, M. Rønning, J. Yang, Core-shell nanostructures of graphene-wrapped CdS nanoparticles and TiO_2 (CdS@G@TiO_2): the role of graphene in enhanced photocatalytic H_2 generation. Catalysts **10**, 358 (2020). https://doi.org/10.3390/catal10040358

129. S. Bai, J. Ge, L. Wang, M. Gong, M. Deng et al., A unique semiconductor–metal–graphene stack design to harness charge flow for photocatalysis. Adv. Mater. **26**, 5689–5695 (2014). https://doi.org/10.1002/adma.201401817

130. D.V. Dao, G.D. Liberto, H. Ko, J. Park, W. Wang et al., $LaFeO_3$ meets nitrogen-doped graphene functionalized with ultralow Pt loading in an impactful Z-scheme platform for photocatalytic hydrogen evolution. J. Mater. Chem. A **10**, 3330 (2022). https://doi.org/10.1039/d1ta10376h

131. X. Fan, G. Zhang, F. Zhang, Multiple roles of graphene in heterogeneous catalysis. Chem. Soc. Rev. **44**, 3023 (2015). https://doi.org/10.1039/c5cs00094g

132. X. Qu, Q. Hu, Z. Song, Z. Sun, B. Zhang et al., Adsorption and desorption mechanisms on graphene oxide nanosheets: Kinetics and tuning. The Innovation **2**, 100137 (2021). https://doi.org/10.1016/j.xinn.2021.100137

133. Y. Yang, M. Liu, S. Han, H. Xi, C. Xu et al., Double-sided modification of TiO_2 spherical shell by graphene sheets with enhanced photocatalytic activity for CO_2 reduction. Appl. Surf. Sci. **537**, 147991 (2021). https://doi.org/10.1016/j.apsusc.2020.147991

134. Y. Zhao, Y. Wei, X. Wu, H. Zheng, Z. Zhao et al., Graphene-wrapped Pt/TiO_2 photocatalysts with enhanced photogenerated charges separation and reactant adsorption for high selective photoreduction of CO_2 to CH_4. Appl. Catal. B-Environ. **226**, 360–372 (2018). https://doi.org/10.1016/j.apcatb.2017.12.071

135. M. Zhang, M. Wu, Z. Wang, R. Cheng, D.Y.C. Leung et al., Efficient sunlight driven CO_2 reduction on Graphene-wrapped $Cu-Pt/rTiO_2@SiO_2$. Mater. Sci. Energy Technol. **3**, 734–741 (2020). https://doi.org/10.1016/j.mset.2020.09.001

136. L. Pei, Y. Yuan, W. Bai, T. Li, H. Zhu et al., In situ-grown island-shaped hollow graphene on TaON with spatially separated active sites achieving enhanced visible-light CO_2 reduction. ACS Catal. **10**, 15083–15091 (2020). https://doi.org/10.1021/acscatal.0c03918

137. Y.-H. Chen, J.-K. Ye, Y.-J. Chang, T.-W. Liu, Y.-H. Chuang et al., Mechanisms behind photocatalytic CO_2 reduction by $CsPbBr_3$ perovskite-graphene-based nanoheterostructures. Appl. Catal. B-Environ. **284**, 119751 (2021). https://doi.org/10.1016/j.apcatb.2020.119751

138. P. Kumar, C. Joshi, A. Barras, B. Sieber, A. Addad et al., Core–shell structured reduced graphene oxide wrapped magnetically separable $rGO@CuZnO@Fe_3O_4$ microspheres as superior photocatalyst for CO_2 reduction under visible light. Appl. Catal. B-Environ. **205**, 654–665 (2017). https://doi.org/10.1016/j.apcatb.2016.11.060

139. L. Wang, H. Tan, L. Zhang, B. Cheng, J. Yu, In-situ growth of few-layer graphene on ZnO with intimate interfacial contact for enhanced photocatalytic CO_2 reduction activity. Chem. Eng. J. **411**, 128501 (2021). https://doi.org/10.1016/j.cej.2021.128501

140. R. Guo, J. Wang, Z. Bi, X. Chen, X. Hu et al., Recent advances and perspectives of core-shell nanostructured materials for photocatalytic CO_2 reduction. Small **19**, 2206314 (2023). https://doi.org/10.1002/smll.202206314

141. L. Qi, Z. Zheng, C. Xing, Z. Wang, X. Luan et al., 1D nanowire heterojunction electrocatalysts of $MnCo_2O_4/GDY$ for efficient overall water splitting. Adv. Funct. Mater. **32**, 2107179 (2022). https://doi.org/10.1002/adfm.202107179

142. H. Sun, C. Jing, W. Shang, F. Wang, M. Zeng et al., Polyoxometalate-based composite cluster with core–shell structure:

143. $Co_4(PW_9)_2$@graphdiyne as stable electrocatalyst for oxygen evolution and its mechanism research. New J. Chem. **46**, 11553 (2022). https://doi.org/10.1039/d2nj01459a

143. J. He, X. Miao, Y. Wu, Z. Jin, Phosphating core–shell graphdiyne/CuI/Cu_3P S-scheme heterojunction confirmed with in situ XPS characterization for efficient photocatalytic hydrogen production. Catal. Sci. Technol. **13**, 5610 (2023). https://doi.org/10.1039/d3cy00850a

144. B. Zhai, H. Li, G. Gao, Y. Wang, P. Niu et al., A crystalline carbon nitride based near-infrared active photocatalyst. Adv. Funct. Mater. **32**, 2207375 (2022). https://doi.org/10.1002/adfm.202207375

145. H. Wang, X. Liu, P. Niu, S. Wang, J. Shi et al., Porous two-dimensional materials for photocatalytic and electrocatalytic applications. Matter **2**, 1377–1413 (2020). https://doi.org/10.1016/j.matt.2020.04.002

146. H. de Lasa, B. Serrano, M. Salaices, *Photocatalytic reaction engineering* (Springer, New York, 2005)

147. S. Barata-Vallejo, S.M. Bonesi, A. Postigo, Photocatalytic fluoroalkylation reactions of organic compounds. Org. Biomol. Chem. **13**, 11153 (2015). https://doi.org/10.1039/c5ob01486g

148. F. Zhang, X. Wang, H. Liu, C. Liu, Y. Wan et al., Recent advances and applications of semiconductor photocatalytic technology. Appl. Sci. **9**, 2489 (2019). https://doi.org/10.3390/app9122489

149. J. Chen, J. Shi, X. Wang, H. Cui, M. Fu, Recent progress in the preparation and application of semiconductor/graphene composite photocatalysts. Chin. J. Catal. **34**, 621–640 (2016). https://doi.org/10.1016/s1872-2067(12)60530-0

150. Y. Guo, X. Tong, N. Yang, Photocatalytic and electrocatalytic generation of hydrogen peroxide: principles, catalyst design and performance. Nano-Micro Lett. **15**, 77 (2023). https://doi.org/10.1007/s40820-023-01052-2

151. M.G. Lee, J.W. Yang, H. Park, C.W. Moon, D.M. Andoshe et al., Crystal facet engineering of TiO_2 nanostructures for enhancing photoelectrochemical water splitting with $BiVO_4$ nanodots. Nano-Micro Lett. **14**, 48 (2022). https://doi.org/10.1007/s40820-022-00795-8

152. P. Zhang, Y. Zhao, Y. Li, N. Li, S.R.P. Silva et al., Revealing the selective bifunctional electrocatalytic sites via in situ irradiated X-ray photoelectron spectroscopy for lithium–sulfur battery. Adv. Sci. **10**, 2206786 (2023). https://doi.org/10.1002/advs.202206786

153. Y. Li, Y. Zhang, R. Hou, Y. Ai, M. Cai et al., Revealing electron numbers-binding energy relationships in heterojunctions via in-situ irradiated XPS. Appl. Catal. B-Environ. Energy **356**, 124223 (2024). https://doi.org/10.1016/j.apcatb.2024.124223

Publisher's Note Springer Nature remains neutral with regard to jurisdictional claims in published maps and institutional affiliations.